Atomic-scale microstructure of metal halide perovskite

Authors: Mathias Uller Rothmann[1], Judy S. Kim[2,3,4], Juliane Borchert[1], Kilian Lohmann[1], Colum M. O'Leary[2], Alex Sheader[2], Laura Clark[2], Henry J. Snaith[1], Michael B. Johnston[1], Peter D. Nellist[2], and Laura M. Herz[1]*

Affiliations:

[1]Department of Physics, University of Oxford, Clarendon Laboratory, Parks Road, Oxford OX1 3PU, UK

[2]Department of Materials, University of Oxford, Parks Road, Oxford OX1 3PH, UK

[3]ePSIC, Diamond Light Source, Harwell, Didcot, OX11 0DE, UK

[4]Rosalind Franklin Institute, Fermi Ave, Harwell, Didcot, OX11 0QS, UK

*Correspondence to: laura.herz@physics.ox.ac.uk

One Sentence Summary:
The atomic-scale microstructure of metal halide perovskites is revealed by high-resolution, low-dose electron microscopy.

Abstract:

Hybrid organic-inorganic perovskites are exciting materials for solar-energy applications whose microscopic properties are still not well understood. Atomic-resolution (scanning) transmission electron microscopy, (S)TEM, has provided invaluable insights for many crystalline solar-cell materials, and is used here to successfully image $CH(NH_2)_2PbI_3$ thin films with low electron-radiation dose. Such images reveal a highly ordered atomic arrangement of sharp grain boundaries and coherent perovskite/PbI_2 interfaces, with a

striking absence of long-range disorder in the crystal. We demonstrate that beam-induced degradation of the perovskite leads to an initial loss of $CH(NH_2)_2^+$ ions, leaving behind a partially unoccupied perovskite lattice, which explains the unusual regenerative properties of these materials. We further observe aligned point defects and climb-dissociated dislocations. Our findings thus provide an atomic-level understanding of technologically important lead-halide perovskites.

Main Text:

Many of the phenomenal advances in the performance of hybrid metal halide perovskite (MHP) solar cells have resulted from improvements in device architecture and material composition studied on a mesoscopic to macroscopic scale[1-7], and changes in material properties have usually been inferred from relatively "large area" probes[8-11]. While these probes are able to resolve properties on the scale of a few hundred nanometres to a few millimetres, the mechanisms behind the impressive performance of hybrid perovskites have yet to be fully understood, and are bound to link directly with unique properties at the atomic level. This point is vividly illustrated by effects such as the gradual rather than abrupt decrease in photovoltaic performance of MHPs over time[12], their readily regenerative properties when exposed to gaseous iodo-organic precursors[13], and the counterintuitively beneficial effects of adding a small excess (2 %[14, 15]-7.5 %[16]) of PbI_2 to the MHP precursor solution. Similarly, significant efforts have been made to describe the properties of grain boundaries in MHP thin films using light and scanning probes[17-19] with highly inconsistent results[11, 17]. Recent work has shown that a smaller spread of grain boundary orientations increases the photoluminescence intensity locally[20], but the exact atomic nature of grain boundaries has still not been described. Even the crystal phase of the technologically important $CH(NH_2)_2PbI_3$ (formamidinium lead iodide, $FAPbI_3$) MHP is still uncertain[21]. Therefore, truly atomic

resolution imaging of metal halide perovskites has phenomenal potential to provide urgently needed understanding for a plethora of puzzling observations already established for perovskite devices, and in turn, boost their efficiencies further. In addition, grain boundaries have been postulated to have a significant impact on the long-term stability of MHPs(*22, 23*), yet their exact nature is still mostly unknown.

These examples illustrate that a detailed understanding of the atomic structure of MHPs is urgently required in order to address these fundamental issues and allow further development of perovskite solar cells and other optoelectronic technologies. Atomic-resolution transmission electron microscopy has uniquely answered similar questions for other crystalline solar cell materials(*24, 25*), but the highly beam-sensitive nature of hybrid perovskites makes high-resolution electron microscopy extremely challenging. While fully inorganic photoactive perovskites have been successfully imaged(*26*), the few studies observing the pristine hybrid perovskite phase are based on nanostructures(*27, 28*), and no studies of pristine, native hybrid perovskite thin films have to date been published. Unstable under electron beams, MHPs rapidly change into a more stable PbI_2 phase under even mild electron irradiation(*29, 30*), which has resulted in significant differences in the crystallography reported by electron microscope and X-ray studies(*11*).

Imaging the perovskite structure

We employ low-dose scanning transmission electron microscopy to obtain images of pristine $FAPbI_3$, as STEM has been shown for other materials to produce less damage with the same total electron fluence (dose)(*31*). In order to resolve both "near-stoichiometric" polycrystalline $FAPbI_3$ films, and those formed with significant excess PbI_2 precursor ("PbI_2-rich"), we prepared two different types of thermally evaporated materials on ultra-thin carbon-coated copper TEM grids: thinner 30-nm $FAPbI_3$ films close to stoichiometry (FA:Pb:I ratios close to 1:1:3, containing a small excess of PbI_2 as used to optimize for solar cell applications(*32*)) and

thicker 90-nm films containing significant excess PbI_2. To examine whether similar atomic-scale microstructures were also observable for $MAPbI_3$ we also deposited $MAPbI_3$ films of 30 nm thickness containing significant excess PbI_2. Full details of the sample preparation procedures and characterization are provided in the Supplementary Materials and Fig. S1. We have reported thin films of $FAPbI_3$ and $MAPbI_3$ deposited by us from such dual-source vapor-deposition protocols to achieve photovoltaic power conversion efficiencies of 14-19 % when incorporated into suitable device architectures(*23, 33*). STEM samples were annealed according to protocols previously developed to optimize photovoltaic performance. In **Fig. 1** we show a low-angle annular dark field (LAADF, inner radius of 33 mrad, see Methods for full low-dose image acquisition conditions) STEM micrograph of a 90-nm thick $FAPbI_3$ film containing excess PbI_2. LAADF is similar to high-angle annular dark field (HAADF) as it detects scattered electrons, making it sensitive to atomic number variations, but has the advantage of collecting a higher fraction of the scattered electrons, leading to a higher atomic detection efficiency. In addition, LAADF allows efficient imaging of lower-Z elements, which scatter at lower angles(*34*). In order to improve the contrast of this image of a pristine crystal, we applied a Bragg filter, as described in detail the Methods Section and Fig. S2.
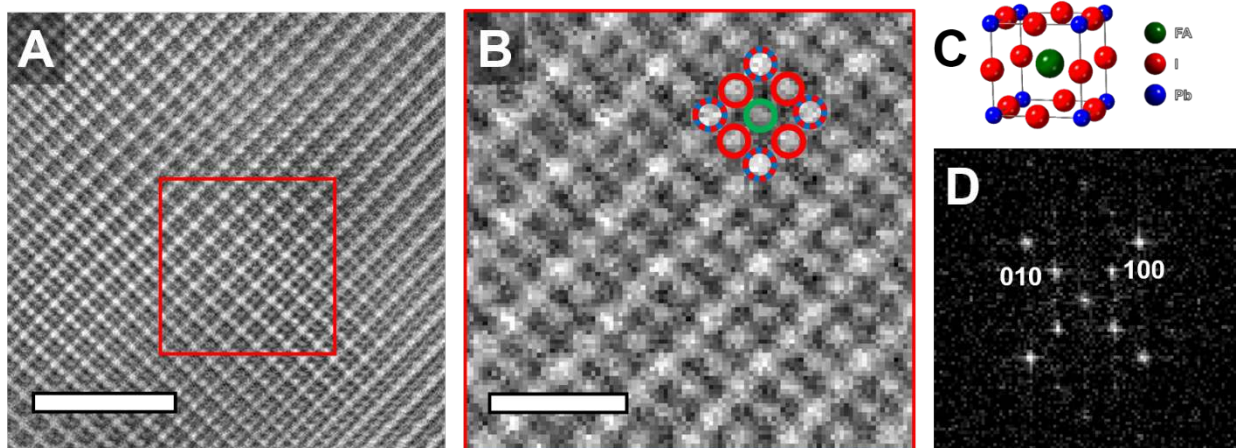

Fig. 1: Atomic resolution imaging of the metal halide perovskite structure. (A) *Bragg-filtered atomic resolution LAADF micrograph of a pristine 90-nm thick, <001>-oriented $FAPbI_3$ film fabricated with excess PbI_2. A distinct pattern in the contrast of the individual atomic columns*

is clearly visible, with the area in the red square magnified in (B). Here, the variations in composition appear as differences in contrast, the dashed blue and red circles showing the Pb/I columns, the red circles showing the pure I columns, and the green circles showing the FA⁺ columns, indicated in the atomic unit cell seen in (C). The Fourier transformation (FT) in (D) confirms the presence of the {010} and {100} planes, which are often missing from atomic-resolution studies of beam-damaged FAPbI₃. The scale bars in (A,B) represent 5 and 1 nm, respectively. The total dose used for acquisition of images (A) and (B) is ~100 e Å⁻². A comparison of the full image, for raw (unfiltered), Butterworth- and Bragg-filtered data is shown in Fig. S2.

The lower magnification image in Fig. 1A reveals an atomic lattice pattern consistent with a cubic structure observed along the <001> orientation. The magnified image in Fig. 1B clearly shows the atomic-level crystal structure corresponding to the cubic structure of room-temperature FAPbI₃, displayed schematically in Fig. 1C(*21*). We note that the preferred alignment of growth along the [100] axis ("face-up") is generally observed by us in these dual-source vapor-deposited films, and is common for lead halide perovskite deposited across a variety of alternative processing techniques(*35*). We also note that an important advantage of LAADF imaging in this case is that, similarly to HAADF imaging, the column intensities retain a monotonic dependence on atomic number. For completeness, a comparison with a HAADF image, acquired as described in the Methods, is shown in Fig. S3.

Three levels of intensity are observable in the LAADF images: the brightest corresponds to the corners of the cubic unit cell (dashed blue and red circles in Fig. 1B), containing alternating lead and iodine, both strongly scattering elements. The second brightest intensity corresponds to the edges of the unit cell containing only iodine, illustrated by the red circles in Fig. 1B. In the *z* viewing direction, the corners make up a total of one lead atom and one iodine per unit

cell, whereas the edge position only contains one iodine, resulting in less scattering and a less bright image intensity. The central, lowest intensity position corresponds to the FA^+ ions, which scatter the least because of their organic nature and singular presence in the centre of the unit cell[34]. Intensity line profiles and a multislice simulation verifying the differences in contrast are provided in Fig. S4.

To support structure identification, we performed a Fourier transformation (FT, shown in Fig. 1D) on the area marked in Fig. 1A, clearly identifying the presence of the (100) and (010) planes along with the (200) and (020) planes. Out of the three proposed room-temperature crystal phases of $FAPbI_3$ (cubic, trigonal, and hexagonal[21]), the spots corresponding to the (100) and (010) planes are unique to the cubic perovskite structure and cannot correspond to either of the other two. This strongly indicates that the room-temperature phase of $FAPbI_3$ is cubic in the $Pm\overline{3}m$ space group.

We note that the (100) and (010) FT spots evident in Fig. 1D have been absent in previous atomic-resolution (S)TEM studies of both $FAPbI_3$ and $MAPbI_3$, with only the supposed (200) and the (020) (plane spacings of 3.181 Å) or other higher index spots still visible[36-39]. Broad-beam diffraction studies carried out on $MAPbI_3$ have explained this apparent absence of lower-order diffraction signatures as the result of structural damage caused by high electron irradiation dosage[29, 30]. Thus, the spots attributed to the second-order diffraction off the perovskite lattice may instead derive from the PbI_2 formed as a decomposition product under intense electron irradiation[40, 41].

Electron-induced decomposition

Using a suitably chosen irradiation dosage, we are indeed able to observe the gradual decomposition of $FAPbI_3$ with electron beam exposure. **Fig. 2A** shows a lower magnification Butterworth-filtered LAADF image of a pristine grain boundary in a 30-nm thick $FAPbI_3$ film close to stoichiometry on a carbon-coated TEM grid after a single scan of the electron beam,

with a total dose of ~ 66 eÅ^{-2}. The subsequent scans were also recorded and are provided in Fig. 2B-D. After three scans (~ 200 eÅ^{-2}), the contrast within the perovskite structure has visibly changed, and after nine scans (~ 600 eÅ^{-2}), the perovskite structure is completely depleted and replaced by a crystal structure with uniform column intensities, displayed in Fig. 2C. Further extensive exposure (~ 1333 eÅ^{-2}) slightly alters this phase into one very similar to 2H-hexagonal PbI_2, displayed in Fig. 2D. This final structure is highly stable, does not change significantly after further exposure and corresponds well to the PbI_2 phase observed by diffraction in broad beam TEM studies([29]). A full crystallographic determination of the phase seen in Fig. 2C is beyond the scope of this study, but Fig. S10 shows how a small distortion of hexagonal PbI_2 can form a structure that projects as a square lattice and forms a coherent epitaxial interface with $FAPbI_3$ as observed in the image data. The FTs in Fig. 2E-H show the degradation process on a crystallographic level: for the pristine perovskite, diffraction spots corresponding to the {100} plane family are initially clearly visible (Fig. 2E). Additional spots appear after brief exposure (orange circles, Fig. 2F), likely corresponding to the ordered loss of formamidinium ions discussed in full detail further below. Continued exposure fully destroys the perovskite structure, transforming it into electron-irradiation-stable PbI_2 concomitant with the disappearance of the {100} plane family of the original perovskite (Fig. 2F), and finally into a structure similar to that of 2H-hexagonal PbI_2 (Fig. 2H).
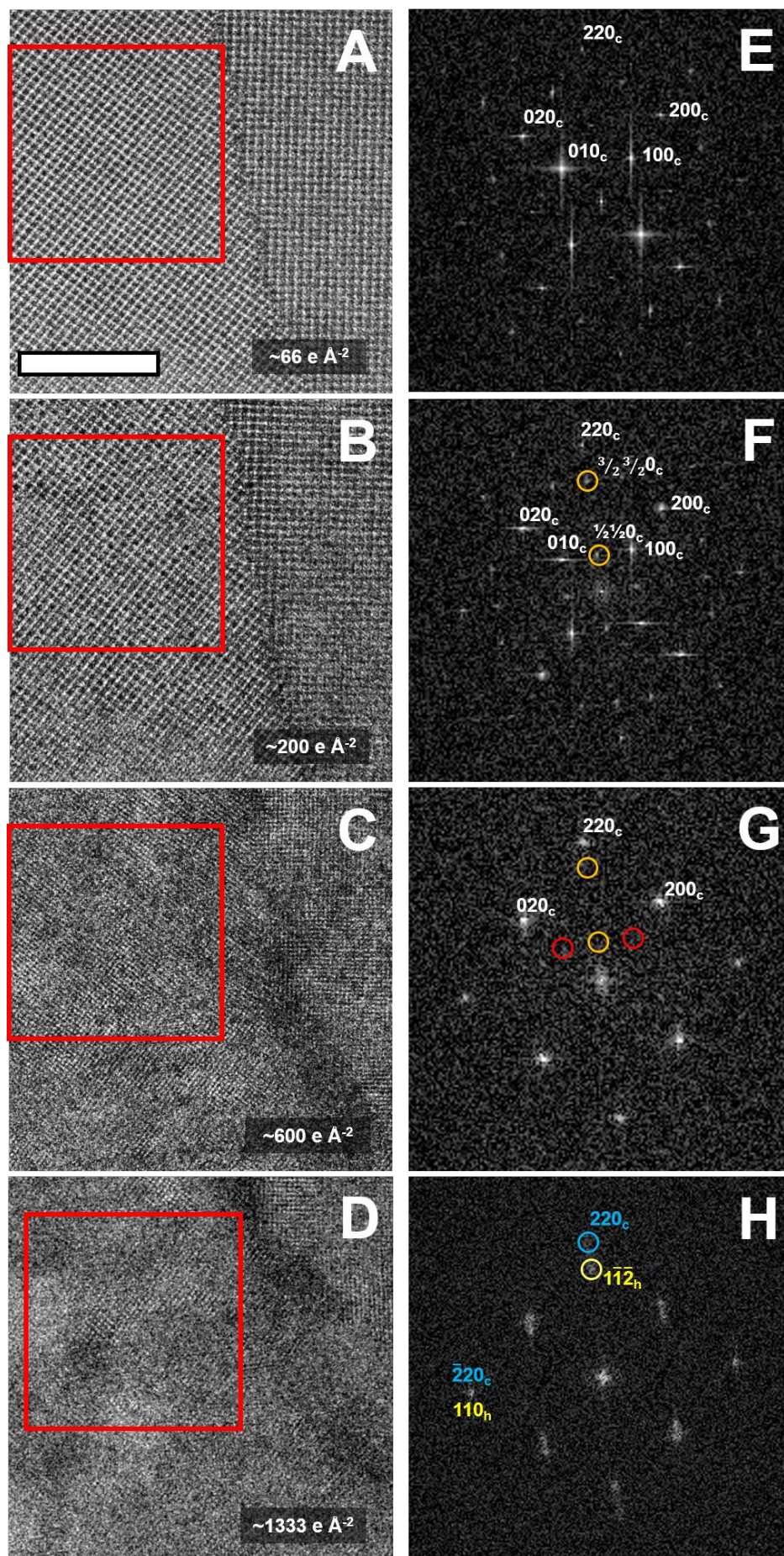
Fig. 2: Damage mechanism of FAPbI₃ under a scanning electron beam observed in a 30-nm thick film prepared near the correct stoichiometry. (A) The first scan (~66 eÅ⁻²) shows the pristine perovskite structure and a grain boundary. (B) After three scans (~200 eÅ⁻²), changes in the crystal structure are apparent in the LAADF image but the grain boundary is still distinguishable. (C) After nine scans (~600 eÅ⁻²) the perovskite structure has fully disappeared and a new crystalline phase has replaced it. Different crystal orientations are visible, but there is no clear grain boundary. (D) After 20 scans (~1333 eÅ⁻²), the angles of the crystal plans change slightly, indicating the complete transformation into 2H-PbI₂. (E-H) show the Fourier transformations corresponding to the areas in the red squares in (A-D), respectively, and confirm the dynamic radiation-induced transformation. Initially, the FT in (E) reveals a pristine cubic structure, but additional spots appear after brief exposure, circled in orange in (F). After further exposure, the additional spots disappear again, along with the {100} spots, whose expected location is marked by red circles in (F). Finally, after extended exposure, the FT contains two sets of spots: one set that can be indexed with the degraded cubic phase and another corresponding to the hexagonal PbI₂-phase, marked with a blue and yellow circle in (G), respectively. The $\bar{2}20_c$ (2.2493 Å) and 110_h (2.2775 Å) spots overlap, indicating an intergrowth of the two phases. Indices marked with a subscript 'c' are from the epitaxial FAPbI₃ phase and those marked with a subscript 'h' are from the hexagonal PbI₂ phase. Note that the material is no longer in its pristine perovskite phase after the initial scan and the 'c' subscript only serves to illustrate the corresponding plane in the pristine phase. The scale bar represents 10 nm and applies to (A-D).

Nanoscopic properties of metal halide perovskites

The implementation of low electron dose, < 200 e Å⁻², inevitably results in a low signal-to-noise ratio when images are recorded. We find that combining low-dose LAADF imaging with

simple Butterworth and Bragg filters allows us to investigate pristine and slightly damaged $FAPbI_3$ thin films with atomic resolution, observing phenomena invisible to other techniques. The details of each filtering technique are provided in the Methods section and in Fig. S5. Our findings are based on hundreds of STEM images taken across 7-8 thin-film samples prepared for each stoichiometry, with the selected images shown in the main section (and further examples provided in the Supplementary Material section) being carefully chosen to be representative of each material's microstructural features. In **Fig. 3** (A-C) we show LAADF STEM images of polycrystalline perovskite films fabricated with excess PbI_2. We observe a surprisingly coherent transition boundary between remnant precursor PbI_2 (highlighted in light orange) and the $FAPbI_3$ grains, with undetectable lattice misfit. In addition, a light and dark chequered pattern becomes clearly visible in images of $FAPbI_3$ after mild radiation damage, as highlighted schematically in the bottom right of Fig. 3A through white and black circles and seen surrounding the PbI_2 region in Fig. 3D. We propose that the observed chequered pattern in the central position of the $FAPbI_3$ unit cell is triggered by an initially random, beam-induced loss of FA^+, likely due to dissociation of the FA^+ by radiolysis[42, 43], potentially complemented by loss of I^- through knock-on (displacement) effects[41, 44]. We postulate that the remaining FA^+ ions then migrate to form an ordered structure with an associated energy reduction that helps stabilise the FA^+ deficient structure. Such migration of FA^+ ions within the perovskite structure after electron irradiation then results in the observed chequered pattern as an intermediate equilibrium[29]. A degradation mechanism assuming solely the ordered loss of I^- has previously been proposed based on analysis of diffraction patterns alone[30], however, we note that this approach struggles to distinguish between ordered loss of FA^+ and I^-. Although vacancy ordering is clearly apparent on the FA^+ sublattice, there is no equivalent effect evident for the I or Pb/I columns (see Fig. S8A for intensity line profiles corresponding to Fig. 3D).

Our direct interpretation of real-space images is thus able to reveal that the degradation is strongly driven by the loss, and likely subsequent reordering, of FA^+ ions.

As further elaborated below, these microstructural features help explain important phenomena pertinent to perovskite solar cells. Specifically, small amounts of PbI_2 are not detrimental to the solar cell performance(*14-16*) since perfect crystallographic alignment between the PbI_2 and $FAPbI_3$ perovskite occurs at the material interface, and no crystal defects are apparent in this region. The observation of the chequered pattern further explains why the perovskite structure can sustain significant deviations from stoichiometry and recover remarkably well from damage.
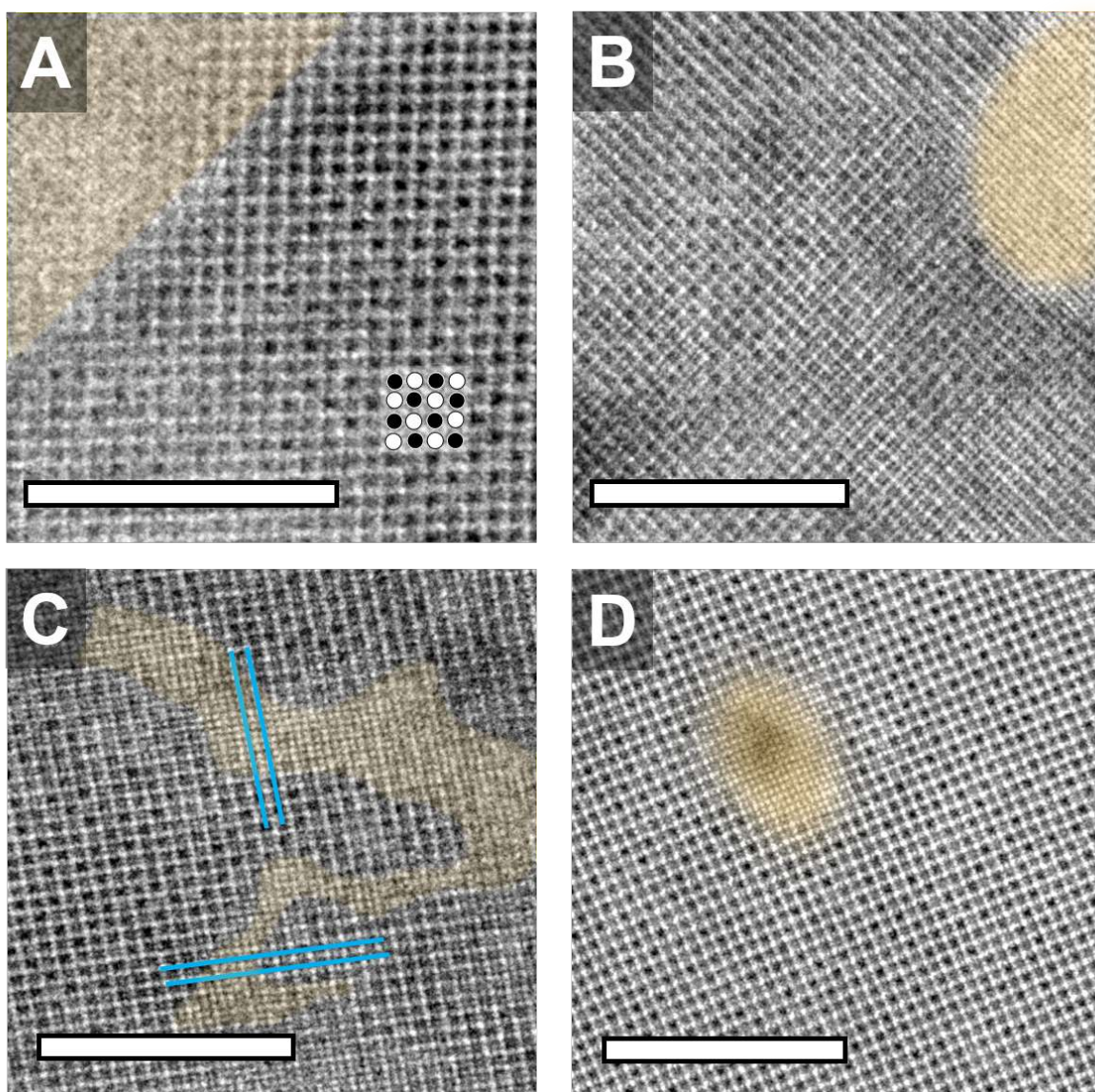
Fig. 3: Atomic-resolution LAADF micrographs of FAPbI₃ thin films showing undistorted transitions between PbI₂ (highlighted in light orange) and FAPbI₃, as well as a chequered intensity after mild radiation damage. *(A-C) show native intergrowth between PbI₂ and FAPbI₃ formed during the deposition process in 90-nm thick FAPbI₃ films fabricated with excess PbI₂, and (D) shows a local area of PbI₂ formation, induced by focusing an electron beam on a near-stoichiometric FAPbI₃ thin film. The highlighted area in (D) corresponds to the damage phase displayed in Fig. 2C and the surrounding area corresponds to that shown in Fig. 2B. The transitions do not induce any measurable phase boundary misfit distortions in the crystal lattice. The nanoscopic PbI₂ domain surrounded by FAPbI₃ in (B) indicates that PbI₂ can act as a seed for growth of FAPbI₃ crystals. The parallel blue lines in (C) begin in a Pb/I lattice site and end in an FA⁺ lattice site after crossing a PbI₂ domain, indicating that areas on either side of the PbI₂ are crystallographically separated and that the presence of PbI₂ is not beam-induced. A chequered pattern in the intensity of the FA⁺ lattice site is visible in (A,C,D), schematically presented as black and white circles in (A). This pattern is indicative of a highly ordered restructuring of the moieties in the crystal after mild electron radiation damage. The Fourier transform of (A) is seen in Fig. S6. All micrographs have been filtered using Butterworth filtering. The scale bars represent 10 nm. The figure is shown without the overlaid colour graphics and with Fourier transforms in Fig. S7.*

We note that at cryogenic temperatures, MAPbI₃ has been shown to amorphise under electron irradiation rather than inducing the gradual, ordered restructuring of the crystal observed at room temperature(*29*). Rothmann *et al*. argued that such amorphisation at low temperatures is the result of impeded ion mobility(*29*), further supporting our notion here that ion migration is a key factor in mitigating the beam induced damage through atomic rearrangement.

We further examine the nature of the native interfaces formed between $FAPbI_3$ and its precursor PbI_2 (Fig. 3). Small amounts of PbI_2 surprisingly do not impede solar cell performance(*14-16*), but the reasons for such benign influence are still a matter of debate. We are able to reveal the presence of a low misfit, low lattice strain interface between $FAPbI_3$ and PbI_2 by examining the intergrowth between $FAPbI_3$ and PbI_2 in a film grown specifically under PbI_2-rich conditions (see Methods). In Fig. 3B a nanoscopic domain of PbI_2 with a continuous transition into $FAPbI_3$ can be seen in the top right-hand corner, with the continuous transition likely arising because of the inclination of the interface to the beam direction. The PbI_2 domain perfectly follows the surrounding perovskite structure and orientation. The lack of evidence for misfit dislocations (see Fig. S9 for more examples) shows that the interface is highly coherent and epitaxial. We note that the known 2H hexagonal phase of PbI_2 could not be coherent with the cubic $FAPbI_3$ in all directions in the interface, but that a modified 2H structure described in Fig. S10 can be coherent with the perovskite, and is possibly stabilised by its interface with $FAPbI_3$ (see Fig. S10 for an atomic model) as evidenced by the square nature of the observed lattice. The weak van der Waals binding between the strongly ionically bound PbI_2 sheets enables the existence of many different PbI_2 polytypes(*45*), and a small shift between the layers of the 2H structure does allow coherent interfaces to form with $FAPbI_3$ (see Fig. S10).(*45*) This coherence also indicates that the PbI_2 has either acted as a seed for the surrounding perovskite or has grown out of the perovskite because of a local lack of FAI.

Further evidence for PbI_2 seeding is revealed in Fig. 3C, where irregularly shaped domains of PbI_2 can be seen to interweave with the perovskite lattice. Here, we observe a shift of half a unit cell in the perovskite crystal across the PbI_2 domain, as evidenced by the two sets of parallel blue lines. These lines are oriented in the <100> direction and begin in an FA^+ lattice site on one side of the PbI_2 domain and end in a Pb/I lattice site on the other side. These columns are not found together on the same {100} plane in a perfect crystal so there must be a relative

shift of half a unit cell on either side of the PbI_2 region. The LAADF signal intensity line profile displayed in Fig. S8B further illustrates this shift across the PbI_2 region. It is unlikely for degradation of $FAPbI_3$ to have resulted in the growth of such an epitaxial PbI_2 phase which exhibits a half-unit-cell distortion of the $FAPbI_3$ matrix, because the low misfit of the interface would not give a driving force for such a distortion of the $FAPbI_3$ structure. We can therefore conclude that the perovskite has grown out of the PbI_2 and not vice versa. Despite this shift, geometric phase analysis (GPA) strain mapping, displayed in Fig. S11, shows an absence of significant strain associated with this perovskite/PbI_2 interface. Fig. S12A,B show examples of both the half a unit cell shift and the PbI_2 intergrowth, respectively, similarly occurring in pristine perovskite that has not suffered electron-beam damage. These observations provide further evidence that the presence of perovskite/PbI_2 intergrowth is not caused by radiation-induced damage, but is an intrinsic property of the material, present from the point of crystal growth. In order to verify that this approach is also applicable to other hybrid perovskites, we also imaged PbI_2-rich $MAPbI_3$ and found similar crystallographic properties, as shown in Fig. S13.

Grain boundaries and crystal defects

We further reveal the nature of the boundaries between individual $FAPbI_3$ grains through high-resolution LAADF imaging. Such grain boundaries are of particular interest for perovskite solar cells since they have been proposed to act both as charge recombination centres(*18, 46, 47*) and conduction pathways(*16*). In addition, grain boundaries have been shown to be intimately linked with the long-term stability of MHPs such as $FAPbI_3$(*22*) and the photo-stability of mixed-halide perovskites towards halide segregation(*23*). Therefore, much effort has been devoted to passivating their negative impact and promoting their positive influence, through appropriate treatments and film growth(*11, 16, 19, 48-51*). While many techniques have been used to infer properties of the grain boundaries in photoactive perovskites(*11, 17*),

reliable imaging with atomic resolution has remained elusive, which has led to some uncertainty about the inherent nature of the boundaries(*17, 51*). A full understanding of the crystallographic nature of grain boundaries is likely to aid an understanding of a plethora of observations already well established in the field of perovskite solar cell devices, leading to further improvements in performance.

Butterworth-filtered LAADF images displayed in **Fig. 4A-C** illustrate a representative set of grain boundaries in an evaporated thin film of $FAPbI_3$, with several striking features. First, the grains are highly crystalline adjacent to the boundaries, showing that the presence of the boundaries does not disrupt the long-range crystal quality of the surrounding perovskite. Secondly, the grain boundaries themselves are clearly defined, with the perovskite structure remaining unchanged to the interface, with no obvious preferred interfacial orientation and typically no amorphous material visible. These two points are illustrated by the strain maps displayed in Fig. S16. While an exhaustive description of the strain associated with all the potential boundaries is beyond the scope of this study, we have mapped the strain associated with the low-angle grain boundary seen in the bottom left of Fig. 4B. We find that the strain is negligible to within one or two unit cells away from the boundary. Along the boundary itself, the strain exhibits a periodic behavior with alternating sign, which arises from the periodic array of edge dislocations forming the grain boundary. The yy strain (lying close to perpendicular to the dislocation burgers vectors) is much lower at the boundary.

Near-120° triple boundaries are commonly observed at the intersection of three grains. Fig. 4A shows a typical image of a triple boundary in a $FAPbI_3$ film, which we generally found to be crystallographically continuous, with minimal lattice distortion and no defects extending away from the grain boundary plane associated with them. Across the STEM micrographs examined, we found this type of "clean" triple boundary to be the most common in $FAPbI_3$, with Fig. S14

providing further examples, as well as an illustration of the wide range of grain boundary angles
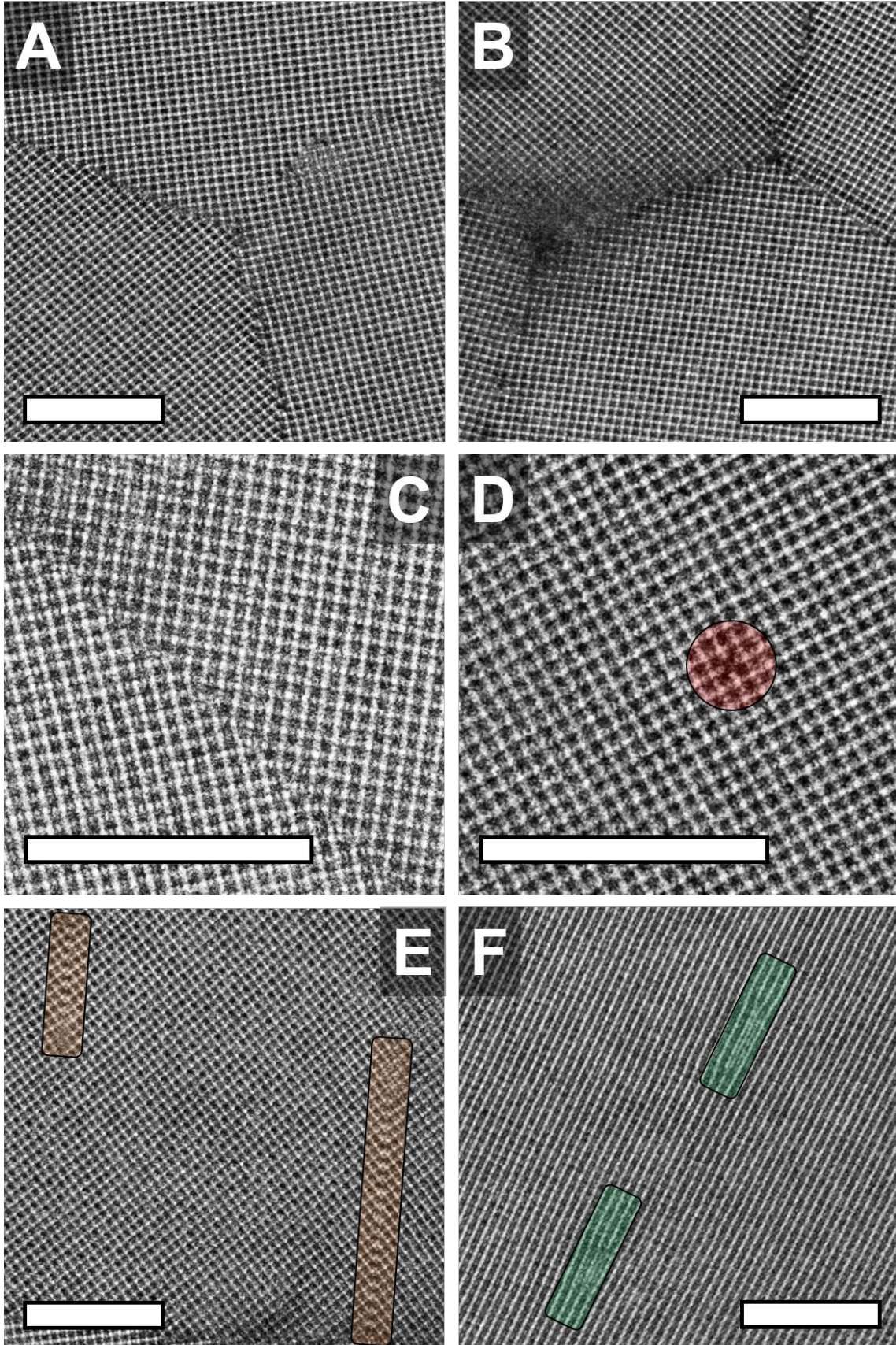
found within the films.

Fig. 4: Butterworth-filtered atomic-resolution LAADF micrographs of representative FAPbI₃ grain boundaries and crystal defects as seen in a 30-nm thick film prepared close to the correct stoichiometry. *(A) Abrupt grain boundaries meeting at a triple junction showing no amorphous or intergranular phase. (B) A triple junction showing signs of amorphisation in the left-hand intersection and a line of vacancies at the right-hand intersection. The boundaries appear randomly oriented, with the presence of a curved boundary in (B) visible in the top right-hand corner. The low-angle grain boundary in the lower left of the image are formed of a series of <100> edge dislocations. (C) A straight section of a grain boundary with virtually no empty lattice sites and very little distortion across the boundary. (D) Aligned vacancy defects on the I/Pb lattice site are seen in the red circle. (E) Intrinsic stacking faults are seen in the orange rectangles with a stacking fault vector of ½<110>. (F) Edge dislocations are seen in the green rectangles with a burgers vector of <100>. The dislocations can be seen to have dissociated in the climb direction forming two ½<100> partial dislocations and a fault lying perpendicular to the glide plane. The scale bars represent 10 nm. The figure is shown without the coloured highlights in Fig. S15.*

Interestingly, while most grain boundaries in these evaporated FAPbI₃ films appear to be highly ordered and sharp, some exceptions also occur. For example, the triple boundary displayed in Fig. 4B contains amorphous material and aligned point defects, as seen in the left-hand and right-hand sides, respectively. Such variation in the nature of grain boundaries observed here for FAPbI₃ may thus also explain the disparity in the grain boundary properties reported in MAPbI₃, ranging from detrimental(*18, 46, 47*) to beneficial(*16*), or even both(*11, 17*). If a particular preparation method favors a particularly beneficial or detrimental type of grain boundary it can improve or decrease solar cell performance, respectively.

Finally, we uncover the presence of aligned point defects and stacking faults in $FAPbI_3$. The nature and distribution of crystal defects in photoactive perovskites is a topic which has received significant attention, but the exact nature of these defects is still unclear[41]. Most studies and simulations have focused on point defects and their influence on charge-carrier properties[52]. As revealed in Fig. 4D, aligned point defects in the form of vacancies on the FA^+ sub-lattice are indeed present in the $FAPbI_3$ crystal. We find here that stacking faults and edge dislocations, displayed in Fig. 4E,F, respectively, are also very common in $FAPbI_3$. Interestingly, the stacking faults shown in Fig. 4E correspond to a shift of half a unit cell, connecting Pb-I columns with I^- columns rather than with FA^+ columns. Edge dislocations are also present, as highlighted in the green rectangles in Fig. 4F. The dislocations are dissociated in a direction perpendicular to their glide plane, and are thus referred to as climb dissociated, with an apparent region of PbI_2 forming the planar fault joining the dislocations.

Discussion

Resolving the atomic structure of $FAPbI_3$ thin films allows us to explain many of the intriguing and unique properties of MHPs that had already been well established in the literature, but lacked an explanation to date. The observed loss of FA^+ through an intermediate perovskite structure displaying a chequered FA^+ vacancy pattern provides a direct clue to the ability for metal halide perovskites to sustain significant deviations in stoichiometry, and the regenerative capacity of hybrid organic-inorganic MHPs. This mechanism is likely to be general, given that gradual changes have also been observed in photoluminescence and cathodoluminescence spectra when MHPs are exposed to photon[53] and electron[54] irradiation, respectively, which do not occur in all-inorganic photoactive perovskites[54]. It is also bound to underpin the readily regenerative properties of photobleached $MAPbI_3$ solar cells when they are exposed to gaseous MAI[13], showing that the lead-iodide perovskite framework remains even after a significant loss of the organic A-cation. This highly adaptable and resilient structure can thus

accommodate dramatic stoichiometry changes without collapsing, which, along with its potential for regeneration, is a clear advantage for applications. Such resilience of structure, induced by ion migration, may well be unique to metal halide perovskites, as compared to other more covalent crystalline solids, and is likely to be the origin of the "radiation hardness" of metal halide perovskites, beckoning well for their use in space applications and as gamma and X-ray detectors.

In addition, the observed atomically coherent nature of perovskite/PbI_2 interfaces explains how the presence of PbI_2 can enhance the crystal quality of MHP films(*16*) by acting as seeds for crystal growth, while not adversely affecting the local optoelectronic properties of the material. Higher-energy charge carriers generated in PbI_2 can easily transfer to the lower-energy perovskite, contributing to the overall photogenerated current(*55*) which is relatively unaffected by the perovskite/PbI_2 boundaries. The highly ordered nature of the perovskite/PbI_2 boundary is therefore a core mechanism underpinning the facile fabrication of high-performance solar cells. In essence, this feature forms the MHP analogue of the native SiO_2-Si interface, which is benign and is probably the main reason why our electronics industry is primarily based on silicon.

The presence of predominantly sharp, strain-free boundaries between individual $FAPbI_3$ grains is a vital clue to the reasons for the high performance of perovskite solar cells based on polycrystalline films. Grain boundaries in other polycrystalline semiconductor solar cells are generally detrimental to performance, decreasing the short-circuit current density and introducing trap states(*56, 57*). The revelation of such sharp boundaries in evaporated $FAPbI_3$ films, with some amorphous exceptions, therefore presents a first step towards understanding the exact nature of grain boundaries in perovskite solar cells, through which improved control can ensure the highest possible solar cell performance and stability. In addition, our acquisition of truly atomic-resolution images, enabled through careful choices of image acquisition and

filtering approaches, will form the basis of investigations into the microstructure of MHPs across a wide range of different stoichiometries. For example, addition of small fractions of Cs to replace some of the FA cations in FAPbI$_3$ has been shown to enhance material stability and crystallinity(*58*), which may link with the nature of grain boundaries.

Finally, stacking faults have been shown to act as recombination sites in dislocation-free silicon(*59*), and edge dislocations decrease the PL intensity in multicrystalline silicon(*60*). Our identification of aligned point defects in the form of vacancies on the FA$^+$ sub-lattice and climb-dissociated dislocations in FAPbI$_3$ provides first insights into the specific forms such defects take in MHPs. Such information will pave the way for future modelling of defects based on first principles, which can reveal the impact such defects have on the optoelectronic properties of metal halide perovskites, and the subsequent performance of perovskite solar cells.

In conclusion, using low-dose LAADF STEM imaging, we are able to obtain atomic-resolution micrographs of pristine cubic FAPbI$_3$ films. We show that electron irradiation causes the perovskite structure to change through an initial loss of the FA$^+$ ion, leaving behind a resilient, partially empty but ordered perovskite lattice, which deteriorates to PbI$_2$ under further irradiation. This intermediate step explains the surprising regenerative properties of radiation-damaged perovskite films, highlighting the highly adaptive nature of the perovskite structure. We further examine the film microstructure, showing that PbI$_2$ precursor remnants readily and seamlessly intergrow with the perovskite lattice, with an atomically continuous co-existence of the two materials within grains. We image FAPbI$_3$ grain boundaries, revealing that the long-range perovskite structure is preserved up to the grain boundaries, where sharp interfaces are generally present, and finally we identify a number of different crystal defects in the perovskite lattice. These findings reveal several mechanisms underpinning the remarkable performance of metal halide perovskites and pave the way for obtaining atomically localised information

from metal halide perovskites, enabling control over these materials for optoelectronic and solar energy applications at a hitherto unseen level.

Methods and Materials

Sample preparation

Both $FAPbI_3$ and $MAPbI_3$ thin films were deposited on the carbon-coated side of 300-mesh copper TEM grids. Immediately prior to deposition, the grids were O_2-plasma cleaned for 0.3 minutes.

$CH(NH)_2I$ (FAI) and PbI_2 were co-evaporated in a customised thermal evaporation chamber described previously(*61*). Heating of the sources started once the chamber pressure fell below 5×10^{-6} mbar. The PbI_2 rate was kept constant at 0.23 Å/s, measured using a gold-plated quartz microbalance (QMB). For the "PbI_2-rich" $FAPbI_3$ films with significant excess of PbI_2, the FAI rate was set to 40 % of the rate used for the "near-stoichiometric" $FAPbI_3$ films. This resulted in FAI crucible temperatures of around 150 °C during the deposition of the PbI_2-rich $FAPbI_3$ films and 180 °C during the deposition of the near-stoichiometric $FAPbI_3$ films. During deposition, the pressure increased to $1\text{-}2 \times 10^{-5}$ mbar for the PbI_2-rich $FAPbI_3$ films, and to $5\text{-}9 \times 10^{-5}$ mbar for the near-stoichiometric $FAPbI_3$ films. The duration of the overall perovskite deposition was controlled such that the film thickness was 90 nm for the PbI_2-rich $FAPbI_3$ films and 30 nm for the near-stoichiometric $FAPbI_3$ films. After deposition, all films were annealed at 170 °C for 1 min. The films were stored in a nitrogen-filled glove box after preparation and transported to the microscope in a triple-sealed nitrogen atmosphere to prevent exposure to moisture.

$CH_3NH_3PbI_3$ (MAPbI$_3$) thin films were prepared using a recently published method(32). CH_3NH_3I (MAI, Greatcell) and PbI_2 (99.999% metal base, Sigma-Aldrich) were co-evaporated in the same custom Lesker thermal evaporator chamber. Heating of the sources started once the chamber pressure fell below 5×10^{-6} mbar. During the subsequent evaporation, the pressure increased to $1\text{-}2\times10^{-5}$ mbar. The PbI_2 rate was kept constant at 0.30 Å/s using a gold-plated quartz microbalance, while the MAI temperature was controlled to aim for an overall MAPbI$_3$ deposition rate of 0.45 Å/s, as measured by a quartz microbalance located next to the substrate. For the depositions used in this work, this involved ramping the MAI crucible from 175.1 °C to 175.6 °C over 1070 s, for 1.1 g of MAI initially in the crucible. The substrate was cooled to 0 °C during the deposition; the sensors were cooled to 17 °C.

All samples were loaded rapidly into the microscope, being in contact with air for less than a minute.

Perovskite film thicknesses were determined from calibration of material deposition rates of the two sources according to quartz microbalance readings inside the vacuum chamber, supported by film depositions on hard transparent quartz substrates for which film thickness readings were determined from a combination of Dektak profilometer readings and optical transmission measurements.

Image acquisition

Microscopy for imaging and condition development was performed on two microscopes. A JEOL ARM-200F cold FEG, C_s probe corrected STEM at 80 or 200 kV acceleration voltage, 20-21 mrad convergence angle, using an annular dark field detector at 8 cm camera length,

resulting in inner and outer collection angles of 33 and 120.77 mrad, respectively for LAADF imaging and 72.80 and 235.75 mrad for HAADF imaging. A JEOL ARM-300F C_s probe corrected STEM at 300 kV was used for imaging condition development. Both room temperature and cryogenic conditions were examined, and the cryogenic conditions did not noticeably reduce the beam sensitivity of the $FAPbI_3$ thin films, so all imaging was done at room temperature. Similarly, no noticeable difference in beam sensitivity was found between 200 and 300 kV acceleration voltage, but the material was found to damage faster at 80 kV. All imaging presented in the manuscript was at 200 kV. All alignments and focusing were done away from the areas imaged to reduce electron beam-induced damage to the material. All micrographs were obtained without tilting the sample to reduce the beam damage.

The specific image acquisition conditions for all images are listed in Table S1.

References

1. H.-S. Kim *et al.*, Lead iodide perovskite sensitized all-solid-state submicron thin film mesoscopic solar cell with efficiency exceeding 9%. *Scientific Reports* **2**, 591 (2012).
2. M. Liu, M. B. Johnston, H. J. Snaith, Efficient planar heterojunction perovskite solar cells by vapour deposition. *Nature* **501**, 395 (2013).
3. H. Zhou *et al.*, Interface engineering of highly efficient perovskite solar cells. *Science* **345**, 542-546 (2014).
4. N. J. Jeon *et al.*, Solvent engineering for high-performance inorganic–organic hybrid perovskite solar cells. *Nat Mater* **13**, 897-903 (2014).
5. J.-P. Correa-Baena *et al.*, The rapid evolution of highly efficient perovskite solar cells. *Energy & Environmental Science* **10**, 710-727 (2017).
6. M. Saliba *et al.*, Incorporation of rubidium cations into perovskite solar cells improves photovoltaic performance. *Science* **354**, 206-209 (2016).
7. D. P. McMeekin *et al.*, A mixed-cation lead mixed-halide perovskite absorber for tandem solar cells. *Science* **351**, 151-155 (2016).
8. D. W. DeQuilettes *et al.*, Photo-induced halide redistribution in organic–inorganic perovskite films. *Nature communications* **7**, 1-9 (2016).
9. C. C. Stoumpos, C. D. Malliakas, M. G. Kanatzidis, Semiconducting tin and lead iodide perovskites with organic cations: phase transitions, high mobilities, and near-infrared photoluminescent properties. *Inorganic chemistry* **52**, 9019-9038 (2013).

10. T. Baikie *et al.*, A combined single crystal neutron/X-ray diffraction and solid-state nuclear magnetic resonance study of the hybrid perovskites $CH_3NH_3PbX_3$ (X= I, Br and Cl). *Journal of Materials Chemistry A* **3**, 9298-9307 (2015).

11. M. U. Rothmann, W. Li, J. Etheridge, Y. B. Cheng, Microstructural Characterisations of Perovskite Solar Cells–From Grains to Interfaces: Techniques, Features, and Challenges. *Advanced Energy Materials* **7**, (2017).

12. K. Domanski, E. A. Alharbi, A. Hagfeldt, M. Grätzel, W. Tress, Systematic investigation of the impact of operation conditions on the degradation behaviour of perovskite solar cells. *Nature Energy* **3**, 61-67 (2018).

13. L. Hong *et al.*, Improvement and Regeneration of Perovskite Solar Cells via Methylamine Gas Post-Treatment. *Advanced Functional Materials* **27**, 1703060 (2017).

14. D. H. Cao *et al.*, Remnant PbI_2, an unforeseen necessity in high-efficiency hybrid perovskite-based solar cells? *Apl Materials* **2**, 091101 (2014).

15. H.-Y. Hsu *et al.*, Optimization of PbI_2/$MAPbI_3$ perovskite composites by scanning electrochemical microscopy. *The Journal of Physical Chemistry C* **120**, 19890-19895 (2016).

16. Y. C. Kim *et al.*, Beneficial effects of PbI_2 incorporated in organo-lead halide perovskite solar cells. *Advanced Energy Materials* **6**, 1502104 (2016).

17. J.-W. Lee *et al.*, The role of grain boundaries in perovskite solar cells. *Materials Today Energy* **7**, 149-160 (2018).

18. R. Long, J. Liu, O. V. Prezhdo, Unravelling the effects of grain boundary and chemical doping on electron–hole recombination in $CH_3NH_3PbI_3$ perovskite by time-domain atomistic simulation. *Journal of the American Chemical Society* **138**, 3884-3890 (2016).

19. T. Niu *et al.*, Stable High-Performance Perovskite Solar Cells via Grain Boundary Passivation. *Advanced Materials* **30**, 1706576 (2018).

20. S. Jariwala *et al.*, Local crystal misorientation influences non-radiative recombination in halide perovskites. *Joule* **3**, 3048-3060 (2019).

21. C. L. Davies *et al.*, Impact of the organic cation on the optoelectronic properties of formamidinium lead triiodide. *The journal of physical chemistry letters* **9**, 4502-4511 (2018).

22. S. K. Yadavalli *et al.*, Mechanisms of Exceptional Grain Growth and Stability in Formamidinium Lead Triiodide Thin Films for Perovskite Solar Cells. *Acta Materialia*, (2020).

23. A. Knight, L. M. Herz, Preventing phase segregation in mixed-halide perovskites: a perspective. *Energy & Environmental Science*, (2020).

24. O. Breitenstein, J. Rakotoniaina, M. H. Al Rifai, M. Werner, Shunt types in crystalline silicon solar cells. *Progress in Photovoltaics: Research and Applications* **12**, 529-538 (2004).

25. A. Stoffers *et al.*, Complex Nanotwin Substructure of an Asymmetric Σ 9 Tilt Grain Boundary in a Silicon Polycrystal. *Physical review letters* **115**, 235502 (2015).

26. Y. Yu *et al.*, Atomic resolution imaging of halide perovskites. *Nano letters* **16**, 7530-7535 (2016).

27. D. Zhang *et al.*, Atomic-resolution transmission electron microscopy of electron beam–sensitive crystalline materials. *Science* **359**, 675-679 (2018).

28. Y. Li *et al.*, Unravelling degradation mechanisms and atomic structure of organic-inorganic halide perovskites by cryo-EM. *Joule* **3**, 2854-2866 (2019).

29. M. U. Rothmann *et al.*, Structural and chemical changes to $CH_3NH_3PbI_3$ induced by electron and gallium ion beams. *Advanced Materials* **30**, 1800629 (2018).

30. S. Chen *et al.*, Atomic scale insights into structure instability and decomposition pathway of methylammonium lead iodide perovskite. *Nature communications* **9**, 1-8 (2018).

31. R. Hooley, A. Brown, A. Kulak, F. Meldrum, R. Brydson, in *Journal of Physics: Conference Series*. (IOP Publishing, 2017), vol. 902, pp. 012005.

32. K. B. Lohmann *et al.*, Control over crystal size in vapor deposited metal-halide perovskite films. *ACS Energy Letters* **5**, 710-717 (2020).

33. J. Borchert *et al.*, Large-area, highly uniform evaporated formamidinium lead triiodide thin films for solar cells. *ACS Energy Letters* **2**, 2799-2804 (2017).

34. J. Gonnissen *et al.*, Optimal experimental design for the detection of light atoms from high-resolution scanning transmission electron microscopy images. *Applied Physics Letters* **105**, 063116 (2014).

35. L. Oesinghaus *et al.*, Toward tailored film morphologies: the origin of crystal orientation in hybrid perovskite thin films. *Advanced Materials Interfaces* **3**, 1600403 (2016).

36. H. J. Jung *et al.*, Stability of halide perovskite solar cell devices: in situ observation of oxygen diffusion under biasing. *Advanced Materials* **30**, 1802769 (2018).

37. T. W. Kim *et al.*, Self-Organized Superlattice and Phase Coexistence inside Thin Film Organometal Halide Perovskite. *Advanced Materials* **30**, 1705230 (2018).

38. Z. Chen, Z.-G. Gu, W.-Q. Fu, F. Wang, J. Zhang, A confined fabrication of perovskite quantum dots in oriented MOF thin film. *ACS applied materials & interfaces* **8**, 28737-28742 (2016).

39. M. Xiao *et al.*, A Fast Deposition-Crystallization Procedure for Highly Efficient Lead Iodide Perovskite Thin-Film Solar Cells. *Angewandte Chemie* **126**, 10056-10061 (2014).

40. Y. Zhou, H. Sternlicht, N. P. Padture, Transmission electron microscopy of halide perovskite materials and devices. *Joule* **3**, 641-661 (2019).

41. J. Ran *et al.*, Electron-Beam-Related Studies of Halide Perovskites: Challenges and Opportunities. *Advanced Energy Materials*, 1903191 (2020).

42. R. Egerton, Radiation damage to organic and inorganic specimens in the TEM. *Micron* **119**, 72-87 (2019).

43. R. F. Egerton, P. Li, M. Malac, Radiation damage in the TEM and SEM. *Micron* **35**, 399-409 (2004).

44. J. Ran *et al.*, Electron-Beam-Related Studies of Halide Perovskites: Challenges and Opportunities. *Advanced Energy Materials,* **10**, 1903191 (2020).

45. P. A. Beckmann, A review of polytypism in lead iodide. *Crystal Research and Technology* **45**, 455-460 (2010).

46. H.-S. Duan *et al.*, The identification and characterization of defect states in hybrid organic–inorganic perovskite photovoltaics. *Physical chemistry chemical physics* **17**, 112-116 (2015).

47. X. Wen *et al.*, Defect trapping states and charge carrier recombination in organic–inorganic halide perovskites. *Journal of Materials Chemistry C* **4**, 793-800 (2016).

48. D. W. de Quilettes *et al.*, Impact of microstructure on local carrier lifetime in perovskite solar cells. *Science* **348**, 683-686 (2015).

49. Q. Chen *et al.*, Controllable self-induced passivation of hybrid lead iodide perovskites toward high performance solar cells. *Nano letters* **14**, 4158-4163 (2014).

50. Y. Shao, Z. Xiao, C. Bi, Y. Yuan, J. Huang, Origin and elimination of photocurrent hysteresis by fullerene passivation in $CH_3NH_3PbI_3$ planar heterojunction solar cells. *Nature communications* **5**, 1-7 (2014).

51. A. F. Castro-Méndez, J. Hidalgo, J. P. Correa-Baena, The role of grain boundaries in perovskite solar cells. *Advanced Energy Materials* **9**, 1901489 (2019).

52. J. M. Ball, A. Petrozza, Defects in perovskite-halides and their effects in solar cells. *Nature Energy* **1**, 1-13 (2016).

53. A. Merdasa *et al.*, Super-resolution luminescence microspectroscopy reveals the mechanism of photoinduced degradation in $CH_3NH_3PbI_3$ perovskite nanocrystals. *The Journal of Physical Chemistry C* **120**, 10711-10719 (2016).

54. C. Xiao *et al.*, Mechanisms of Electron-Beam-Induced Damage in Perovskite Thin Films Revealed by Cathodoluminescence Spectroscopy. *The Journal of Physical Chemistry C* **119**, 26904-26911 (2015).

55. J. B. Patel *et al.*, Photocurrent spectroscopy of perovskite solar cells over a wide temperature range from 15 to 350 K. *The journal of physical chemistry letters* **9**, 263-268 (2018).

56. J. D. Zook, Effects of grain boundaries in polycrystalline solar cells. *Applied Physics Letters* **37**, 223-226 (1980).

57. F. Greuter, G. Blatter, Electrical properties of grain boundaries in polycrystalline compound semiconductors. *Semiconductor Science and Technology* **5**, 111 (1990).

58. J.-W. Lee *et al.*, Formamidinium and Cesium Hybridization for Photo- and Moisture-Stable Perovskite Solar Cell. *Advanced Energy Materials* **5**, 1501310 (2015).

59. L. Kimerling, H. Leamy, J. Patel, The electrical properties of stacking faults and precipitates in heat-treated dislocation-free Czochralski silicon. *Applied Physics Letters* **30**, 217-219 (1977).

60. T. W. Kim *et al.*, Self-Organized Superlattice and Phase Coexistence inside Thin Film Organometal Halide Perovskite. *Advanced Materials* **30**, 1705230 (2018).

61. J. Borchert *et al.*, Impurity Tracking Enables Enhanced Control and Reproducibility of Hybrid Perovskite Vapor Deposition. *ACS applied materials & interfaces* **11**, 28851-28857 (2019).

Author contributions

M.U.R. designed and carried out the electron microscope studies, and analysed and interpreted data. J.S.K. participated in the EM studies and provided insights in data interpretation and during editing. J.B and K.L. prepared the samples. C.O.L. and A.S. assisted with the EM studies. L.C. performed the multislice simulations. H.J.S. contributed to data analysis and interpretation. M.B.J., P.D.N., and L.M.H. designed the study, interpreted data, and supervised M.U.R., who wrote the manuscript with input from all co-authors.

Competing interests declaration

The authors declare the following competing financial interest: H.J.S. is the Chief Scientific Officer and a Director of Oxford PV Ltd, a company that is commercializing perovskite photovoltaic technologies.

Correspondence

Correspondence and requests for materials should be addressed to L.M.H. or P.D.N.

Data availability

The datasets and numerical analysis sets described in this manuscript are available for download from the Oxford University Research Archive, under the following DOI: [DOI will be supplied upon acceptance to ensure file names correctly match final figure names].

Supplementary Materials:
Figures S1-S16
Table S1
References

Science

AAAS

Supplementary Materials for

Atomic-scale microstructure of metal halide perovskite

Authors: Mathias Uller Rothmann[1], Judy S. Kim[2,3,4], Juliane Borchert[1], Kilian Lohmann[1], Colum M. O'Leary[2], Alex Sheader[2], L. Clark[2], Henry J. Snaith[1], Michael B. Johnston[1], Peter D. Nellist[2], and Laura M. Herz[1]*

Affiliations:

[1]Department of Physics, University of Oxford, Clarendon Laboratory, Parks Road, Oxford OX1 3PU, UK

[2]Department of Materials, University of Oxford, Parks Road, Oxford OX1 3PH, UK

[3]ePSIC, Diamond Light Source, Harwell, Didcot, OX11 0DE, UK

[4]Rosalind Franklin Institute, Fermi Ave, Harwell, Didcot, OX11 0QS, UK

*Correspondence to: laura.herz@physics.ox.ac.uk

This PDF file includes:

Materials and Methods
Figs. S1 to S16
Table S1

Table S1: Overview of the imaging conditions for the images included in this manuscript.

Figure	Beam current	Dwell-time	Pixel size	Total dose per area per scan
1A-B	1.49 pA	1 µs	0.42 Å × 0.42 Å	105 e Å^{-2}
2A-C	1.49 pA	2 µs	0.53 Å × 0.53 Å	66 e Å^{-2}
3A-C	1.49 pA	2 µs	0.35 Å × 0.35 Å	152 e Å^{-2}
3D	1.49 pA	2 µs	0.29 Å × 0.29 Å	221 e Å^{-2}
4A,B,E,F	1.49 pA	2 µs	0.29 Å × 0.29 Å	221 e Å^{-2}
4C	1.49 pA	2 µs	0.42 Å × 0.42 Å	105 e Å^{-2}
4D	1.49 pA	2 µs	0.53 Å × 0.53 Å	66 e Å^{-2}
S2A-C	1.49 pA	1 µs	0.42 Å × 0.42 Å	105 e Å^{-2}
S3A-C	1.49 pA	2 µs	0.53 Å × 0.53 Å	66 e Å^{-2}
S4A	1.49 pA	1 µs	0.42 Å × 0.42 Å	105 e Å^{-2}
S5A-F	1.49 pA	2 µs	0.35 Å × 0.35 Å	152 e Å^{-2}
S7A-C	1.49 pA	2 µs	0.35 Å × 0.35 Å	152 e Å^{-2}
S7D	1.49 pA	2 µs	0.29 Å × 0.29 Å	221 e Å^{-2}
S9A-C	1.49 pA	2 µs	0.53 Å × 0.53 Å	66 e Å^{-2}
S12A-B	1.49 pA	2 µs	0.53 Å × 0.53 Å	66 e Å^{-2}
S13	1.49 pA	2 µs	0.53 Å × 0.53 Å	66 e Å^{-2}
S14A-C	1.49 pA	2 µs	0.29 Å × 0.29 Å	221 e Å^{-2}
S15A,B,E,F	1.49 pA	2 µs	0.29 Å × 0.29 Å	221 e Å^{-2}
S15C	1.49 pA	2 µs	0.42 Å × 0.42 Å	105 e Å^{-2}
S15D	1.49 pA	2 µs	0.53 Å × 0.53 Å	66 e Å^{-2}

Filtering

Butterworth filtering adds a low- or high-pass filter across the Fourier transformation of the real-space image before reconstructing the image from the filtered FT, increasing the contrast of the image uniformly, as seen in Fig. S1B,E(*59, 60*). This approach makes it possible to retain information at grain boundaries, as seen on the left-hand side of Fig. S4B,E, but while it improves the overall contrast ratio dramatically, the noise is also amplified. All of the Butterworth-filtered images in this paper have been filtered using a 1st order filter with a half-point of between 0.02 and 0.05 and a radius of 80.

Bragg filtering imposes a strict periodic mask on the Fourier transformation, only maintaining the signal from a selected set of spots in the FT, as seen in Fig. S1C,F(*61*). This process removes all signal not included in the spots, giving the highest signal-to-noise ratio. This makes the atomic structure very visible, but also removes any features not included in the mask, leading, for example, to weakening of grain boundary information, as seen in Fig. S4C: the right-hand grain has excellent contrast, but the left-hand grain is blurry from the filtering. Choosing the appropriate filtering is, therefore, essential in order for reliable information to be obtainable. If information relating to the local atomic positions in the structure is desired, Bragg filtering should be applied, and where more macroscopic phenomena, such as grain boundaries, are studied, Butterworth filtering is appropriate.

The film area imaged and displayed in Fig. S1A-C contains both pristine and damaged perovskite as evidenced by the chequered pattern most clearly seen in the top right corner of the filtered images, as well as the additional periodicity observed in the Fourier transformations.

LAADF multislice simulation

The multislice simulations were performed using the MUSTEM software(*62, 63*) with a thickness of 30 nm and other parameters chosen to match the experimental LAADF acquisition. Aberrations were assumed to be negligible. The highly mobile FA^+ ion was modelled as a single particle, located at the notional carbon position with mean square displacements from the XRD literature(*64*). Multislice simulations are not able to quantitatively calculate the scattering intensity of the rotating FA^+ ions precisely and as a result, the intensity of the FA^+ columns in Fig. S4D and Fig. S10 is underestimated but the relative locations are correct. The brightness and contrast of the image were adjusted to clearly illustrate the geometry of the material, which however makes the Pb/I columns appear saturated

Geometric phase analysis (GPA) strain map

GPA strain mapping (Fig. S11) was done using the open-source Strain++ program written by Jon Peters(*65*) and based on the algorithm in ref. (*66*). The g-vectors were chosen to correspond to the 200_c and 020_c spots in the Fourier transform and the resulting ε_{xx} strain map was overlaid on the corresponding Butterworth-filtered LAADF image. The strain profile in Fig. S11 B was extracted from the strain map using Digital Micrograph.
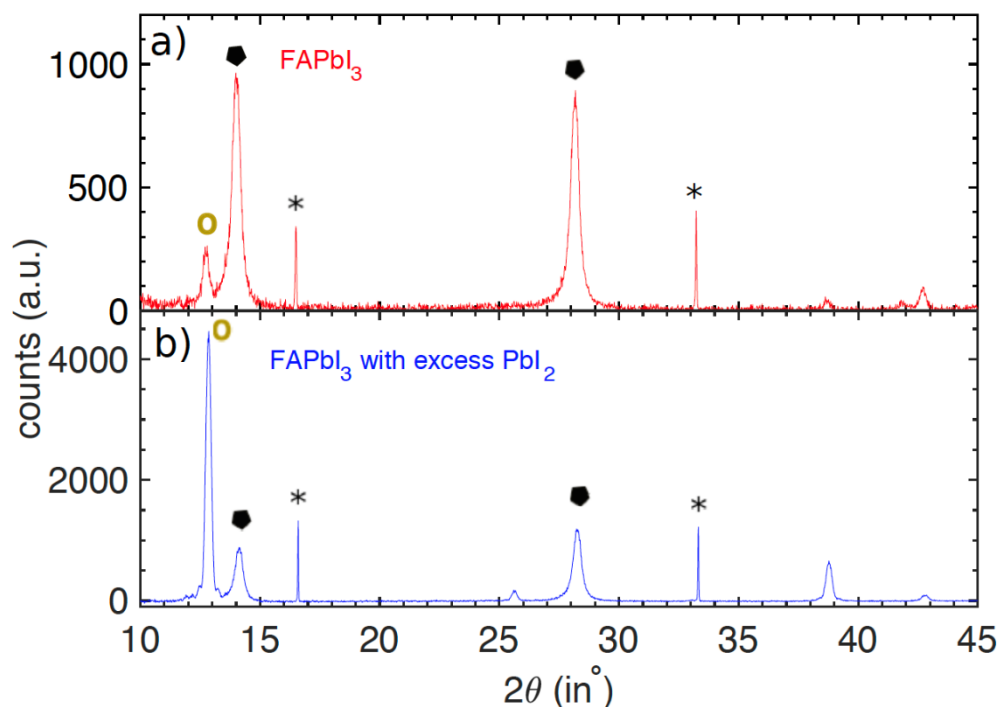
Fig. S1: X-ray diffraction patterns of FAPbI$_3$ films measured with a Panalytical X'pert powder diffractometer for (a) near-stoichiometric FAPbI$_3$ and (b) FAPbI$_3$ deposited under PbI$_2$-rich conditions. Thin-films were deposited from dual-source vapour protocols analogous to those described in the Methods section, but on quartz substrates which allowed for signal to be collected from areas larger than those defined by the copper TEM grids, and facilitated angle calibration with respect to the known quartz diffraction peaks (marked by stars). Film thicknesses were the same as those of the TEM samples. The background was subtracted from the spectra. The characteristic perovskite diffraction peaks (marked by black pentagons) are clearly visible near 14° and 28°. The near-stoichiometry FAPbI$_3$ film only exhibits a small PbI$_2$ diffraction peak (marked by beige circles) while the PbI$_2$-rich FAPbI$_3$ film fabricated with significant excess PbI$_2$ exhibits a much stronger PbI$_2$ peak.
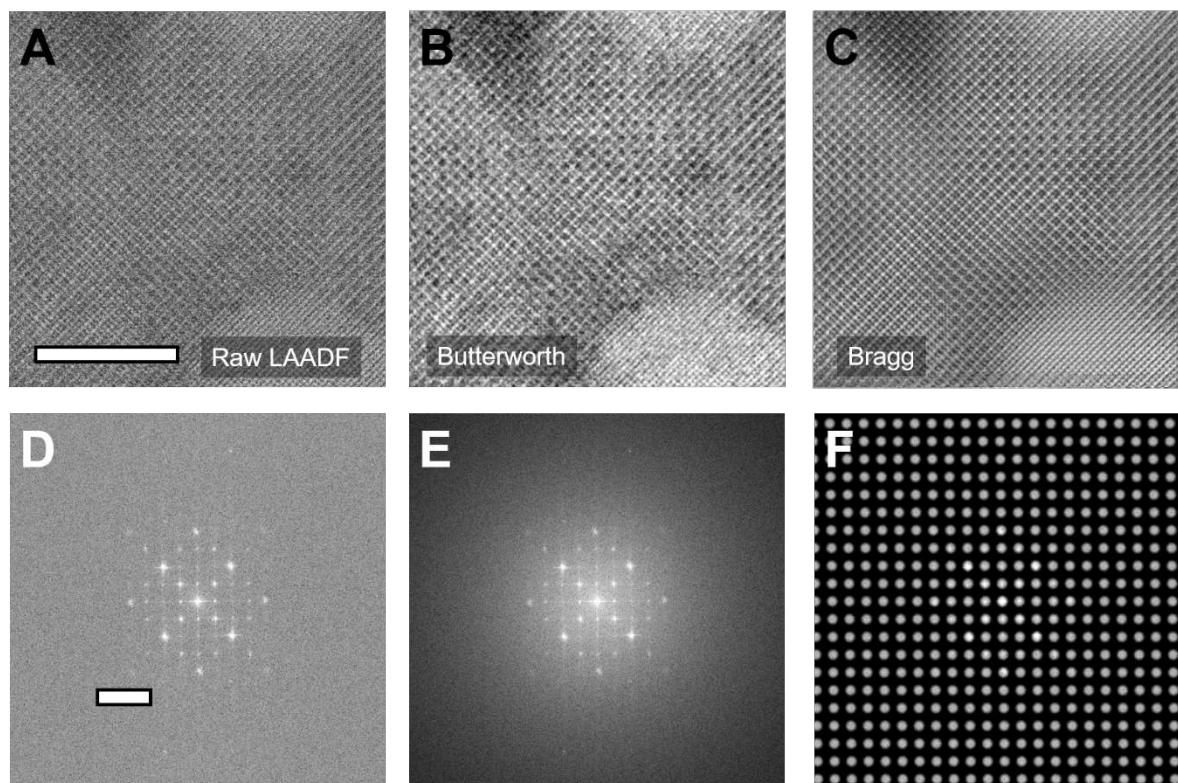
Fig. S2: Different filtering methods and their associated Fourier transformations. (A,D) show the raw LAADF image of an area of a $FAPbI_3$ thin film and its associated Fourier transformation, respectively. (B,E) show the same area and Fourier transformation after a Butterworth low-pass filter has been applied. (C,F) show the same area and Fourier transformation after a Bragg filter has been applied. The real-space scale bar represents 10 nm and applies to (A-C). The Fourier space scale bar represents 4 nm^{-1} and applies to (D-F).
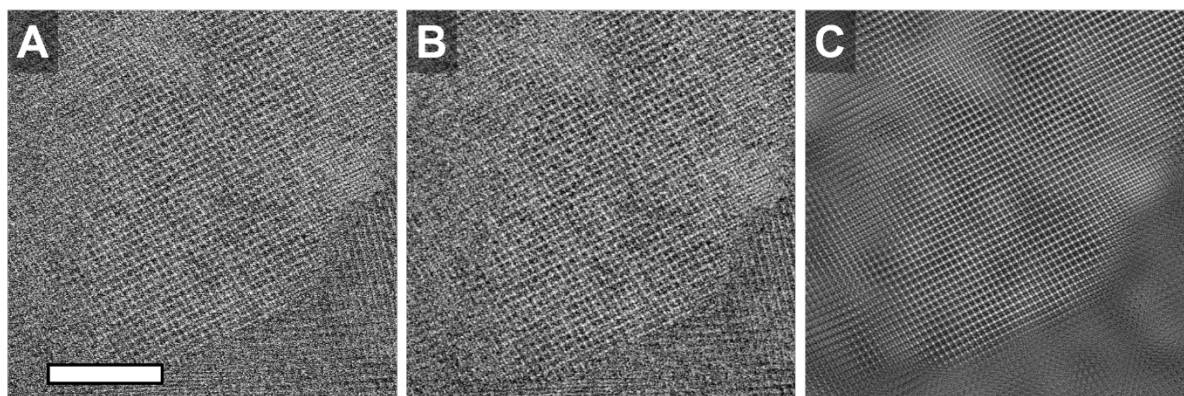
Fig. S3: Atomic-resolution HAADF micrographs of pristine PbI₂-rich FAPbI₃. (A) Raw data, (B) Butterworth filtered, (C) Bragg filtered. Images were obtained using a detector setting with 72.80 and 235.75 mrad as the inner and outer collection angles, respectively. The scale bar represents 10 nm.
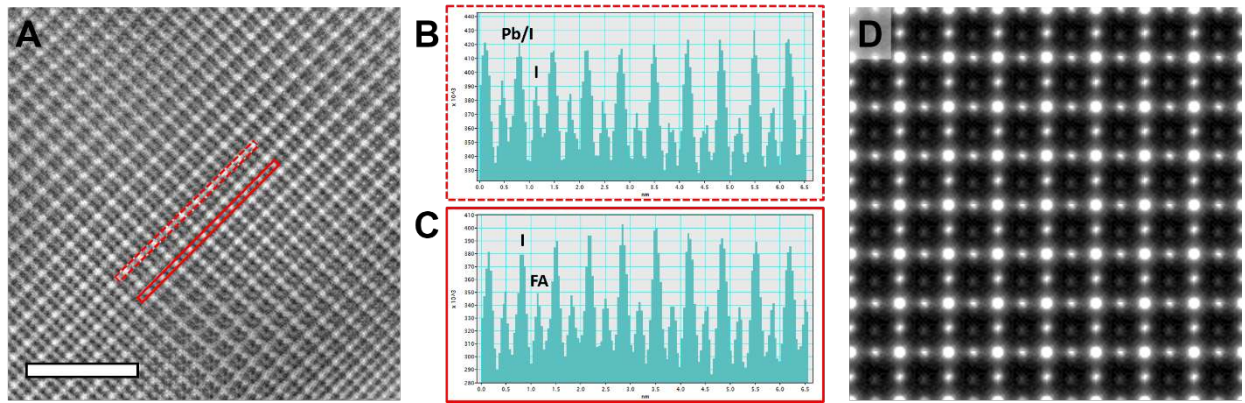
Fig. S4: Intensity line profiles across the Pb/I and the I/FA lattice sites. (A) shows a Bragg-filtered atomic resolution micrograph of a FAPbI$_3$ thin film similar to that displayed in Fig. 1 of the main manuscript. (B,C) show the intensity line profiles obtained from the dashed and solid rectangles in (A), respectively. The scale bar in (A) represents 5 nm. (D) Multislice simulation of the LAADF signal obtained from FAPbI$_3$ when using parameters chosen to match the experimental LAADF acquisition.
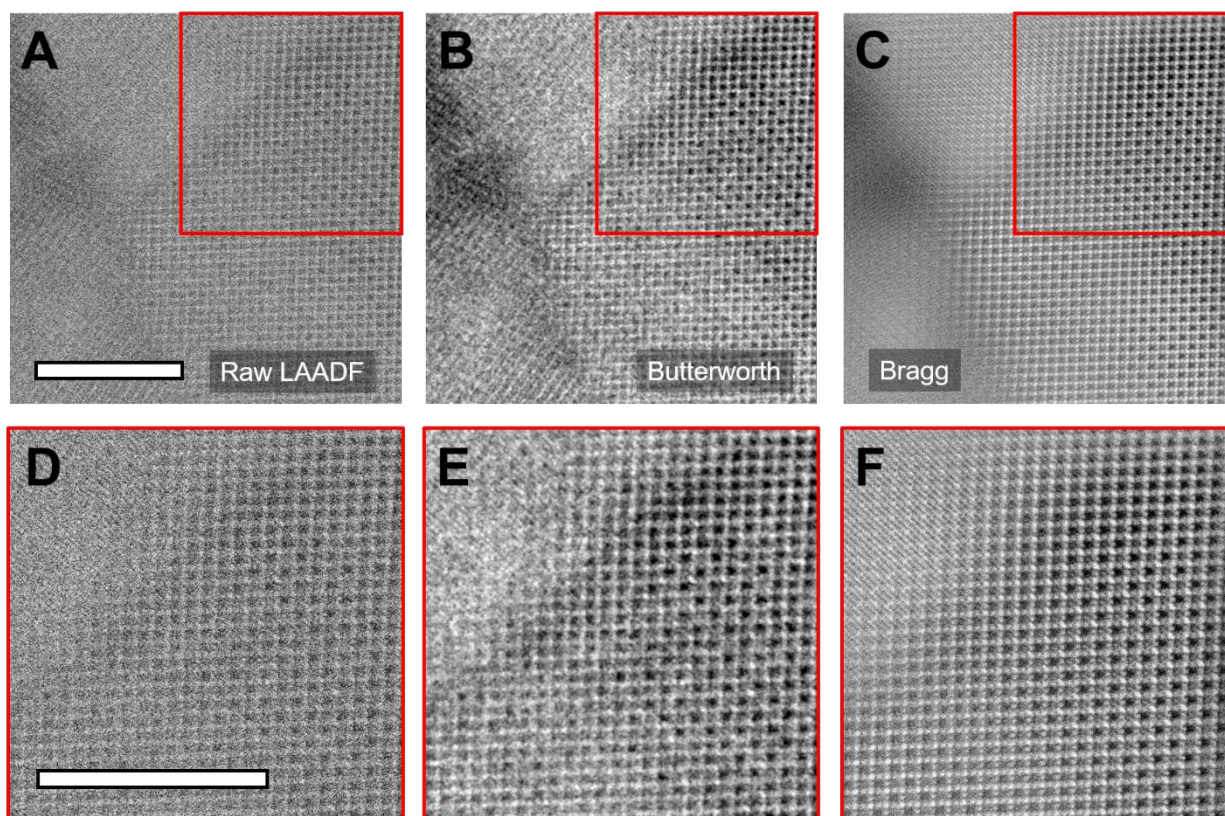
Fig. S5: Atomic-resolution LAADF micrographs of FAPbI$_3$ thin films prepared with excess PbI$_2$ showing a chequered intensity after mild radiation damage and seamless transitions between PbI$_2$ and FAPbI$_3$. (A-C) show real-space LAADF images of a FAPbI$_3$ thin film with (A) no filter applied, (B) a Butterworth low-pass filter applied, and (C) a Bragg filter applied. (D-F) show the corresponding areas marked in the red squares in (A-C). The raw LAADF images are noisy because of the low number of electrons used in order to minimise beam damage. Applying a Butterworth filter dramatically improves the signal-to-noise ratio, making grain boundaries evident. A Bragg filter further improves the signal-to-noise ratio, but does not maintain information from the grain boundaries. Both filters make the PbI$_2$-FAPbI$_3$ intergrowth in the top of the images visible, and the presence of the PbI$_2$ fringes in (F) confirms the close crystallographic relationship between the two phases. Both filters also make the chequered damage pattern in the right-hand grain very visible. The scale bars represent 10 nm.
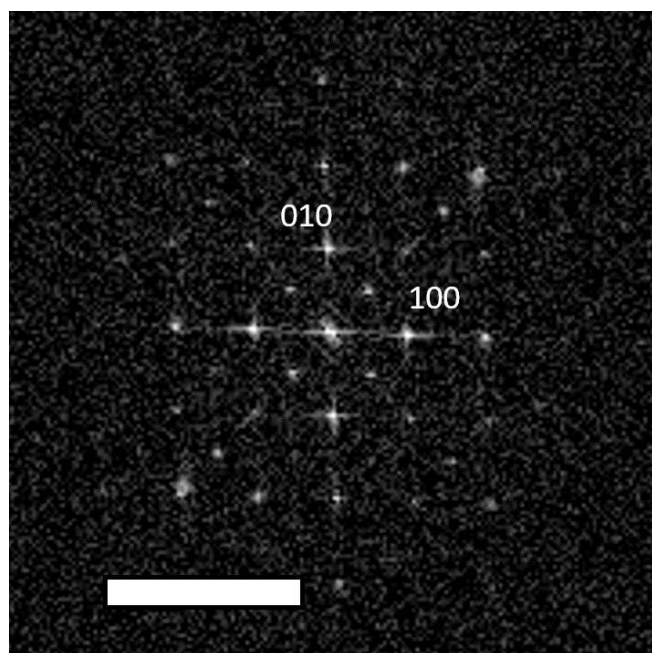
Fig. S6: Fourier transform of Fig. 3A. The scale bar represents 4 nm^{-1}.
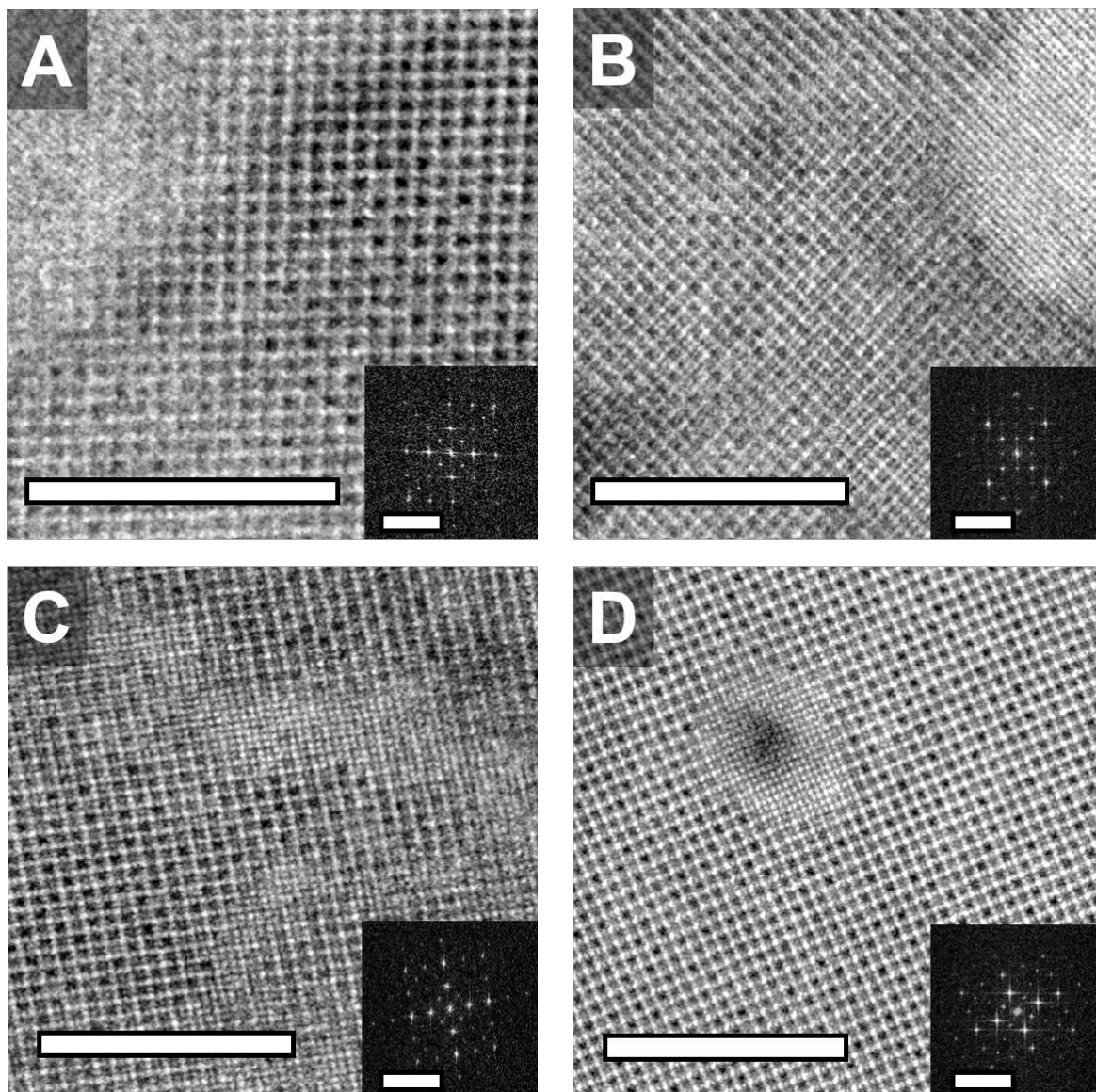
Fig. S7: Atomic-resolution LAADF micrographs of FAPbI₃ thin films showing undistorted transitions between PbI₂ and FAPbI₃, as well as a chequered intensity after mild radiation damage without colour overlay. All micrographs have been filtered using Butterworth filtering. (A-C) were prepared with significant excess PbI_2 and (D) is near-stoichiometric. The inserts show the Fourier transform of the real-space images, illustrating the epitaxial nature of the interfaces. The scale bars represent 10 nm in the real-space images and 4 nm^{-1} in the inserted Fourier transforms.
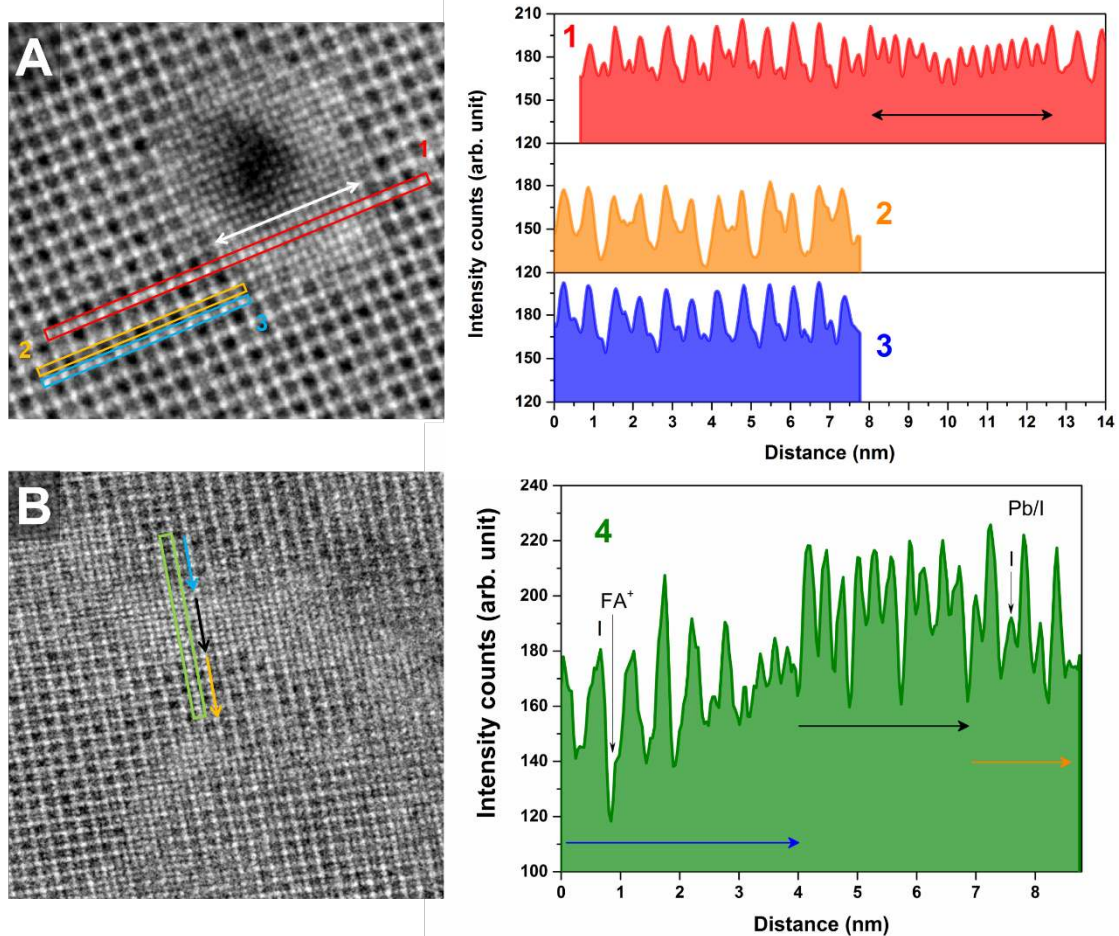
Fig. S8: Intensity line profiles of different atomic columns in FAPbI₃. (A) Line profile 1 (red) shows the intensity variation across Pb/I and I columns of damaged FAPbI$_3$ and the columns in the associated PbI$_2$. The intensity of the signal decreases within the PbI$_2$ region (marked by the black and white arrows), indicating a local loss of material. Line profile 2 (yellow) shows the ordering of the FA$^+$ columns with every other column being either partially or fully empty, indicating a columnar redistribution of the FA$^+$ after beam damage. Line profile 3 (blue) shows minimal evidence of ordered loss of I$^-$, suggesting that the [PbI$_6$] octahedral units can remain intact in the perovskite lattice despite the loss of FA$^+$. (B) Line profile 4 (green) shows the intensity variation across the perovskite/PbI$_2$ intergrowth causing half a unit cell shit, displayed in Fig. 3C. The LAADF signal intensity of the FA$^+$/I columns (blue arrow) is lower than that of the I/Pb:I columns (orange arrow), illustrating the shift of half a unit cell across the PbI$_2$ (black arrow). The composition of the film imaged in (A) is near-stoichiometric, and in (B) as prepared with significant excess PbI$_2$.
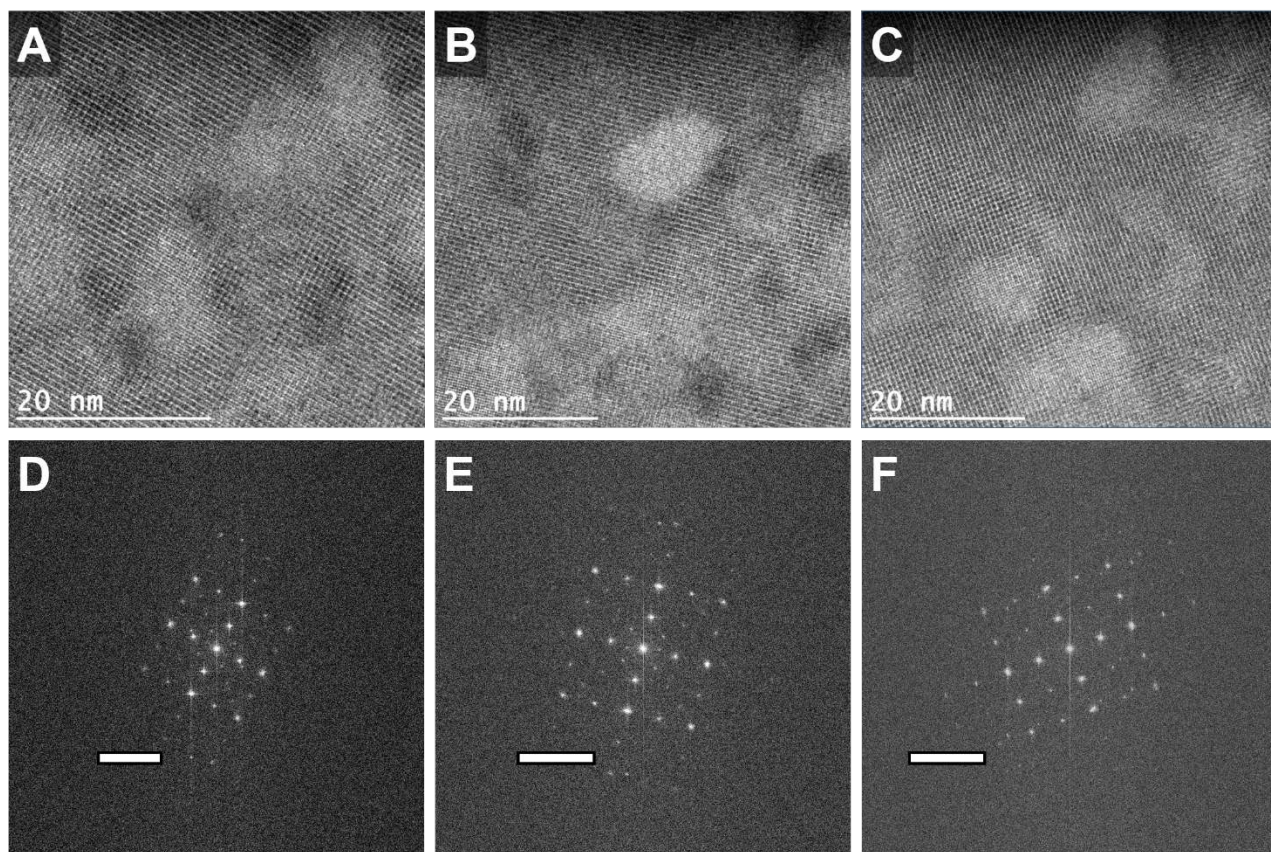
Figure S9: PbI₂ incorporation into FAPbI₃ prepared with significant excess PbI₂. (A-C) Representative Butterworth-filtered LAADF micrographs showing coherent incorporation of PbI₂ clusters into the surrounding perovskite lattice. (D-F) Fourier transforms of the micrographs taken before Butterworth filtering, showing only a single pattern in each transform, indicating that the PbI₂ is incorporated epitaxially into the perovskite lattice in all directions. The scale bars in (D-F) represent 4 nm⁻¹.

FAPbI$_3$ / PbI$_2$ interface

The structure of PbI$_2$ comprises [PbI$_6$] octahedra that form 2D layers which interact through van der Waals forces with neighbouring layers. The I-I distance across the PbI$_2$ octahedra (0.64 nm(*42*)) is very close to the corresponding distance in the similar octahedra in FAPbI$_3$ (0.63 nm). The structure of the 2H polytype viewed along [110] is shown in the top of Fig. S10.

The weak van der Waals interaction between layers leads to extensive polytypism in PbI$_2$ corresponding to various shifts between the layers. The bottom of Fig. S10 shows how a small shift in the registration of the layers and a slight compression of the gap between the layers can lead to a structure that is epitaxial and coherent with the cubic perovskite structure with the [PbI$_6$] octahedra being continuous across the two structures.

This interpretation of the interface structure also explains the relative intensities of the atomic columns in the images in Fig. 3 and Fig. S8. The most intense columns are those in the perovskite with the atomic sequence I-Pb-I-Pb-I-Pb-I. The next most intense columns are those in the PbI$_2$ phase that follow the sequence I-Pb-I-_-I-Pb-I where the underscore is the gap between the layers. They have consistent intensity in both the 2H structure and the distorted epitaxial structure in Fig 2 consistent with our model. The I-_-I-_-I columns in the perovskite follow in the weakening intensity sequence with finally the FA columns being the weakest.
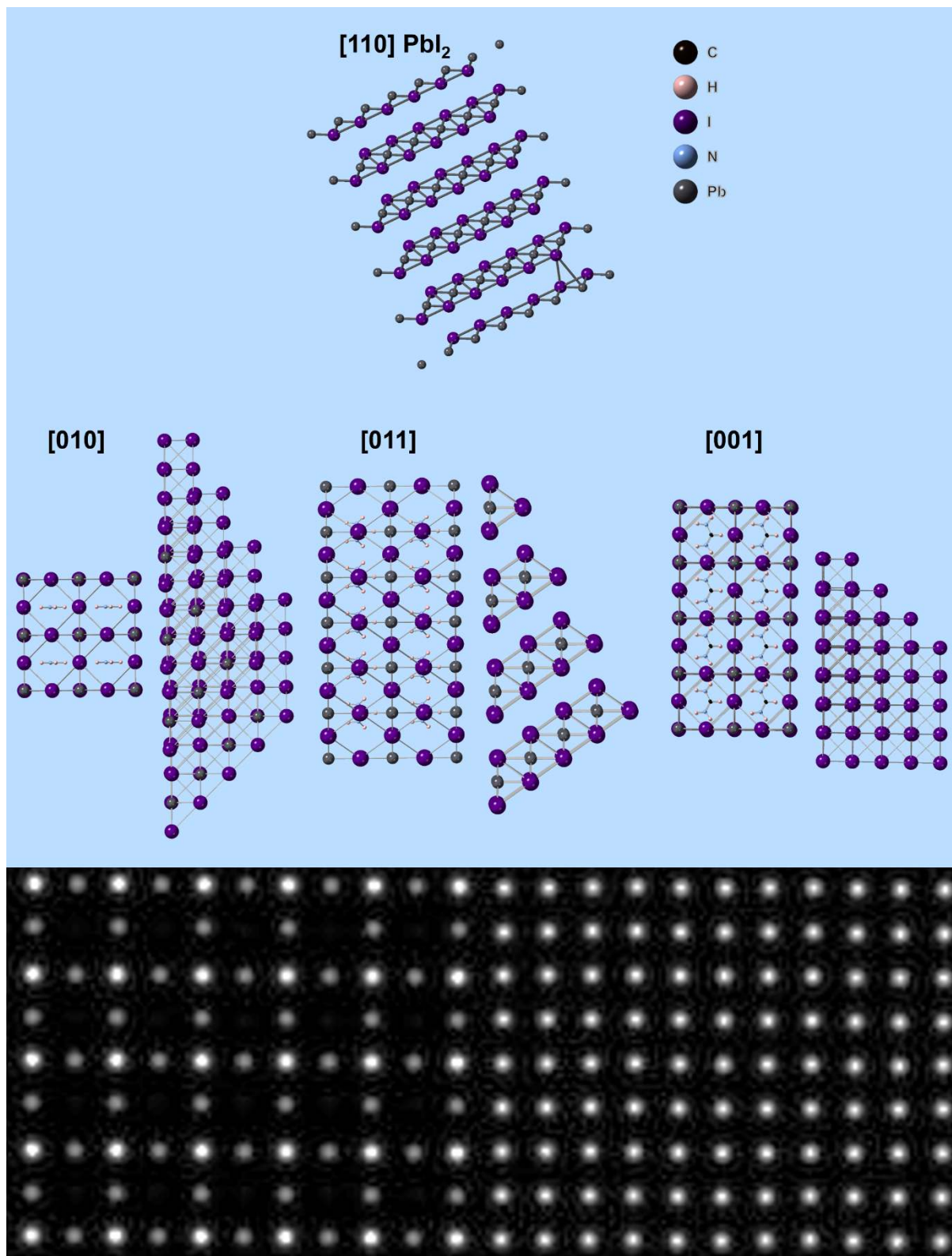
Fig. S10: Stick and ball model of the interface between FAPbI₃ and slightly modified 2H PbI₂ as well as LAADF signal intensity simulation of the interface. Top shows [100]-oriented 2H PbI₂. Middle shows the interface between FAPbI₃ and PbI₂. The interface is shown in three different orientations, with the orientation index corresponding to the FAPbI₃ orientation. The perovskite structure is displayed on the left and the PbI₂ on the right of each interface. Bottom shows the simulated LAADF signal intensity across the interface along the perovskite <100> axis, with the perovskite on the left and PbI₂ on the right. The low intensity

of the FA$^+$ columns caused by the multislice simulations being unable to quantitatively calculate the scattering intensity of the rotating FA$^+$ ions precisely.
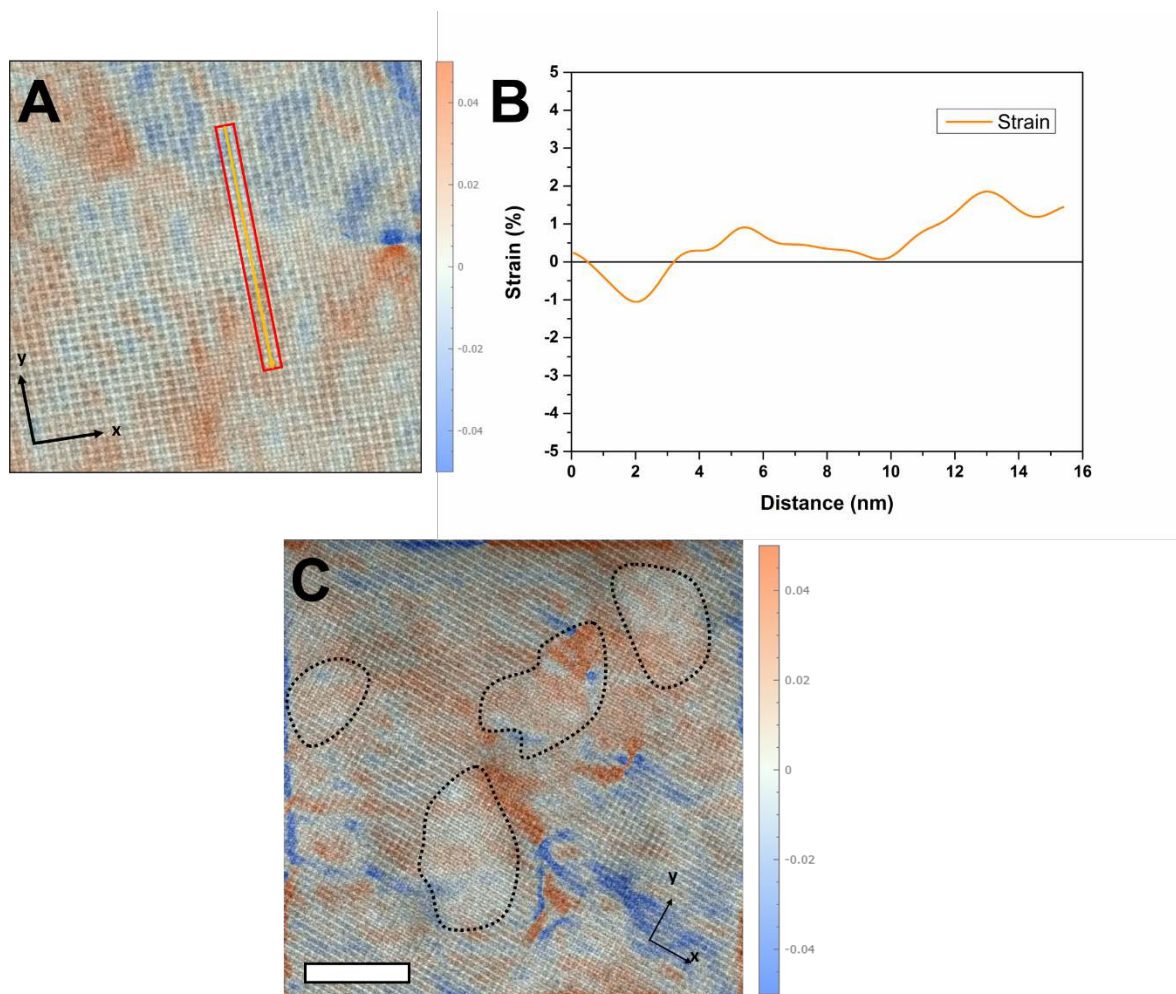

Fig. S11: Crystallographic strain across a PbI$_2$/FAPbI$_3$ interface. (A) Geometric phase analysis heat map of the ε_{xx} strain showing virtually no strain associated with the interface. (B) Line profile of the strain within the red rectangle along the orange arrow. The strain across the interface varies from -1 % to 2 %. (C) Geometric strain analysis heat map of the ε_{yy} strain map in the pristine PbI$_2$-rich FAPbI$_3$ film displayed in Fig. 9A, showing some atomic strain throughout the film. Some PbI$_2$ inclusions are highlighted by the dotted lines, showing that there is no inherently higher strain associated with the PbI$_2$/FAPbI$_3$ interface than within the rest of the film. The scale bar represents 10 nm.
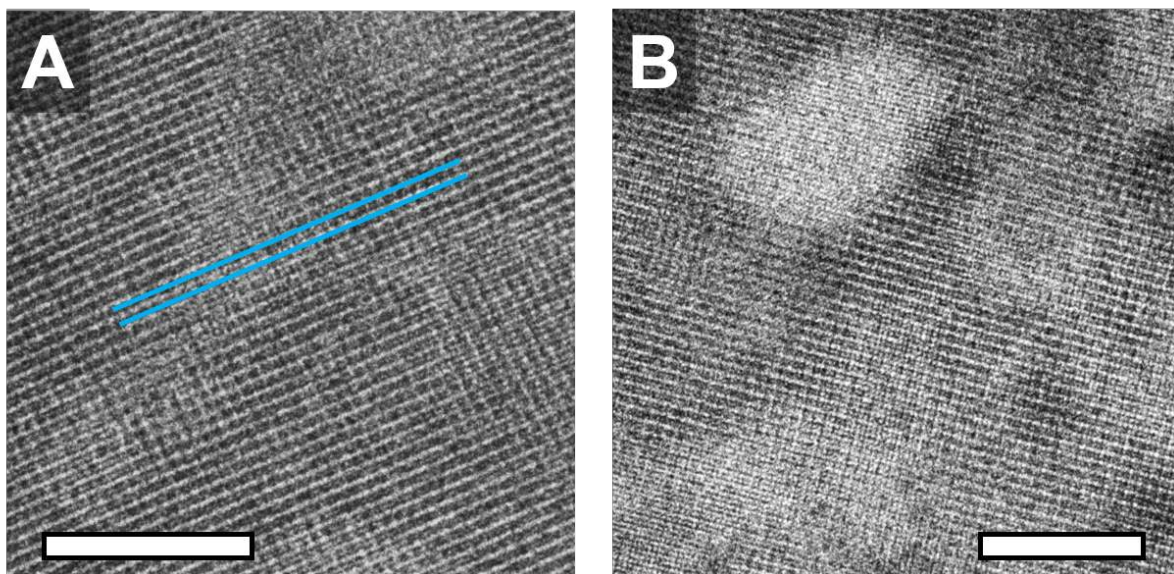
Fig. S12: Atomic-resolution LAADF micrographs of pristine PbI₂-rich FAPbI₃ showing (A) shift of half a perovskite unit cell in pristine FAPbI$_3$ and (B) PbI$_2$ intergrowth with the pristine perovskite lattice. The scale bars represent 10 nm.
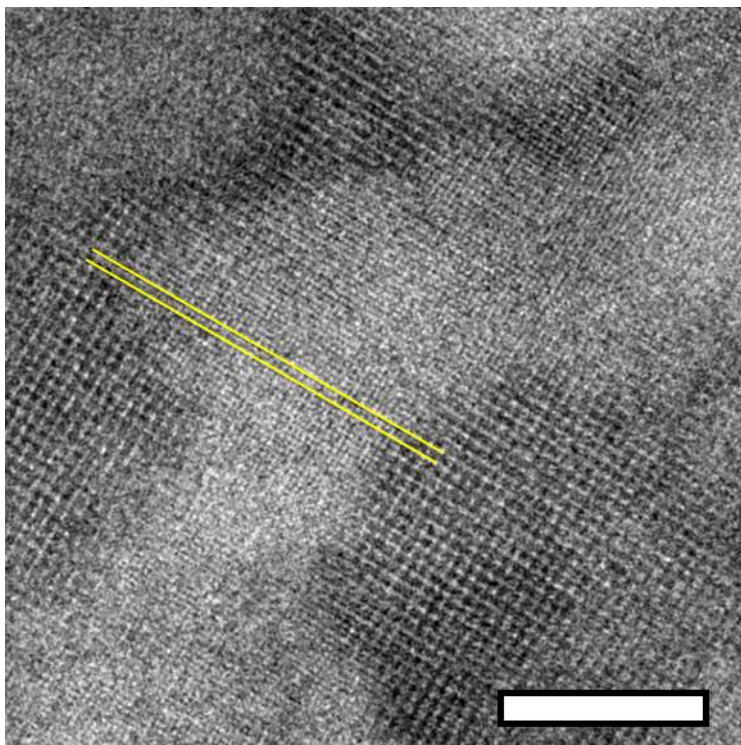
Fig. S13: Atomic-resolution LAADF micrograph of PbI₂-rich MAPbI₃ showing both the undistorted perovskite-to-PbI₂ transitions and the shift of half a unit cell across a PbI₂ region (parallel yellow lines). The scale bar represents 10 nm.
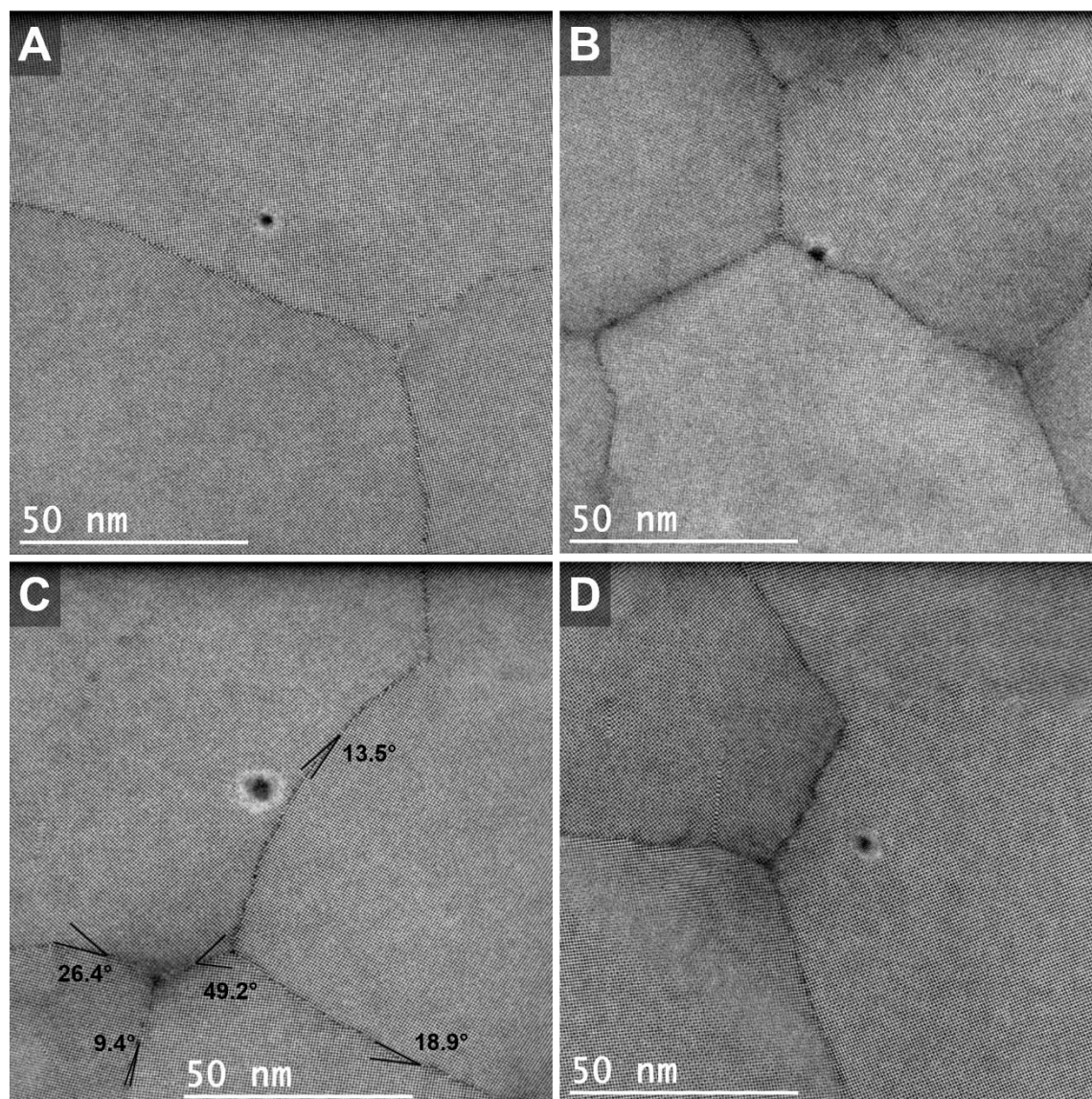
Fig. S14: Representative lower-magnification Butterworth-filtered atomic-resolution micrographs of FAPbI₃ grains as seen in a 30-nm thick film prepared near the correct stoichiometry. The round dark areas are regions damaged by the parked electron beam before image acquisition. Fig. 4A in the main manuscript is a magnified excerpt of (A), Fig. 4B is a magnified excerpt of (C), and Fig. 3D and Fig. 4E are magnified excerpts of (D). A wide range of grain boundary angles are evident in (C), illustrating the highly conformal nature of FAPbI₃.
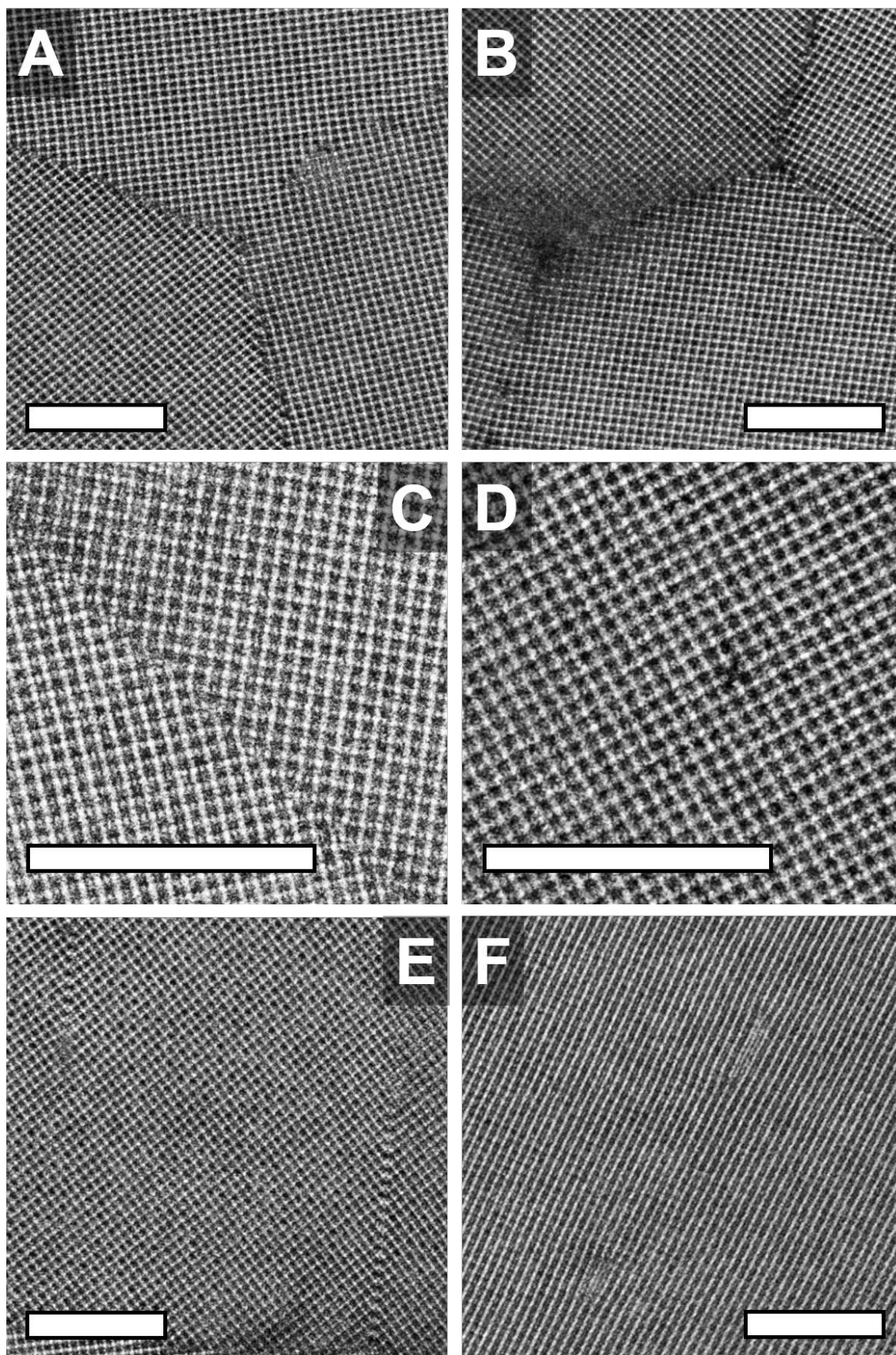
Fig. S15: Butterworth-filtered atomic-resolution micrographs of representative FAPbI₃ grain boundaries and crystal defects as seen in a 30-nm thick film prepared near the correct stoichiometry, shown without colour overlay. The scale bars represent 10 nm.
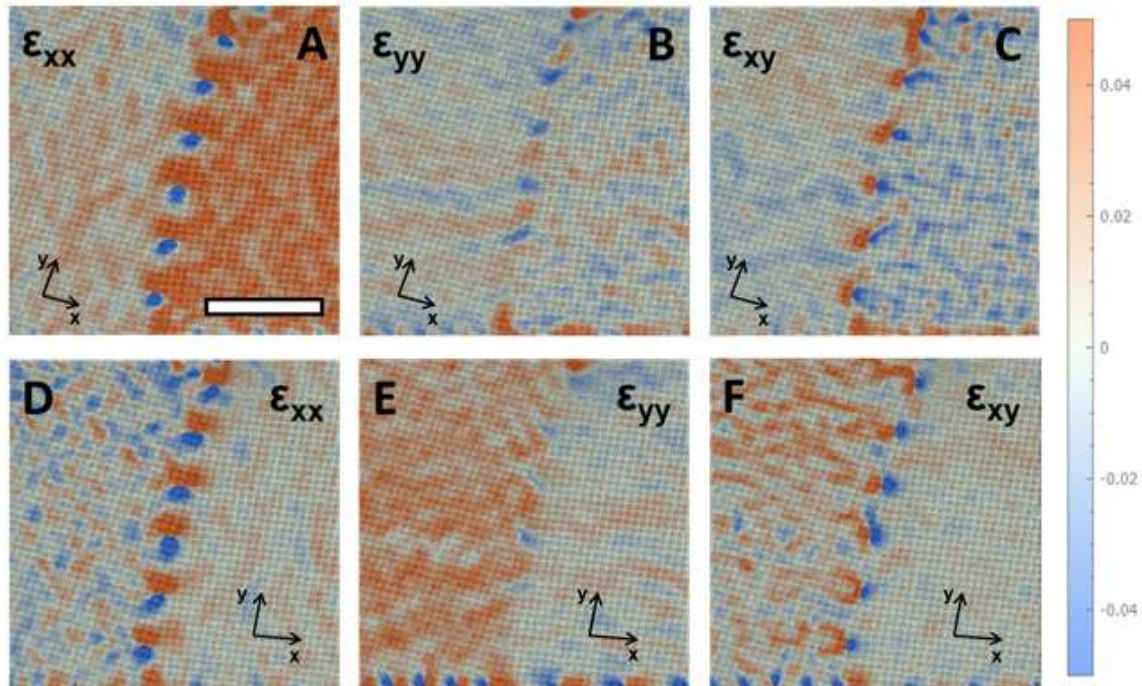
Fig. S16: GPA strain maps near the low-angle boundary between two near-stoichiometric FAPbI3 grains displayed in the bottom left of Fig. 4B. (A-C) show the xx, yy, and xy strain in the left-hand grain, and (D-F) show the xx, yy, and xy strain in the right-hand grain, respectively. A periodic pattern of xx and xy strain with alternating sign is evident and arises from the periodic array of edge dislocations forming the grain boundary, whereas the yy strain (lying close to perpendicular to the dislocation burgers vectors) is much lower at the boundary. All significant strain is localised to within one or two unit cells from the boundary, showing that the boundary does not induce long-range strain in the grains themselves. The inserted coordinate axes show the respective defined lattice directions. The periodic strain patterns at the bottom of each image are due to edge effects and are not physical. The scale bar represents 10 nm and applies to all the images.

References

1. H.-S. Kim *et al.*, Lead iodide perovskite sensitized all-solid-state submicron thin film mesoscopic solar cell with efficiency exceeding 9%. *Scientific reports* **2**, 591 (2012).
2. M. Liu, M. B. Johnston, H. J. Snaith, Efficient planar heterojunction perovskite solar cells by vapour deposition. *Nature* **501**, 395 (2013).
3. H. Zhou *et al.*, Interface engineering of highly efficient perovskite solar cells. *Science* **345**, 542-546 (2014).
4. N. J. Jeon *et al.*, Solvent engineering for high-performance inorganic–organic hybrid perovskite solar cells. *Nat Mater* **13**, 897-903 (2014).
5. J.-P. Correa-Baena *et al.*, The rapid evolution of highly efficient perovskite solar cells. *Energy & Environmental Science* **10**, 710-727 (2017).
6. M. Saliba *et al.*, Incorporation of rubidium cations into perovskite solar cells improves photovoltaic performance. *Science* **354**, 206-209 (2016).
7. D. P. McMeekin *et al.*, A mixed-cation lead mixed-halide perovskite absorber for tandem solar cells. *Science* **351**, 151-155 (2016).
8. D. W. DeQuilettes *et al.*, Photo-induced halide redistribution in organic–inorganic perovskite films. *Nature communications* **7**, 1-9 (2016).
9. C. C. Stoumpos, C. D. Malliakas, M. G. Kanatzidis, Semiconducting tin and lead iodide perovskites with organic cations: phase transitions, high mobilities, and near-infrared photoluminescent properties. *Inorganic chemistry* **52**, 9019-9038 (2013).
10. T. Baikie *et al.*, A combined single crystal neutron/X-ray diffraction and solid-state nuclear magnetic resonance study of the hybrid perovskites CH 3 NH 3 PbX 3 (X= I, Br and Cl). *Journal of Materials Chemistry A* **3**, 9298-9307 (2015).
11. M. U. Rothmann, W. Li, J. Etheridge, Y. B. Cheng, Microstructural Characterisations of Perovskite Solar Cells–From Grains to Interfaces: Techniques, Features, and Challenges. *Advanced Energy Materials* **7**, (2017).
12. K. Domanski, E. A. Alharbi, A. Hagfeldt, M. Grätzel, W. Tress, Systematic investigation of the impact of operation conditions on the degradation behaviour of perovskite solar cells. *Nature Energy* **3**, 61-67 (2018).
13. L. Hong *et al.*, Improvement and Regeneration of Perovskite Solar Cells via Methylamine Gas Post-Treatment. *Advanced Functional Materials* **27**, 1703060 (2017).
14. D. H. Cao *et al.*, Remnant PbI2, an unforeseen necessity in high-efficiency hybrid perovskite-based solar cells? *Apl Materials* **2**, 091101 (2014).
15. H.-Y. Hsu *et al.*, Optimization of PbI2/MAPbI3 perovskite composites by scanning electrochemical microscopy. *The Journal of Physical Chemistry C* **120**, 19890-19895 (2016).
16. Y. C. Kim *et al.*, Beneficial effects of PbI2 incorporated in organo-lead halide perovskite solar cells. *Advanced Energy Materials* **6**, 1502104 (2016).
17. J.-W. Lee *et al.*, The role of grain boundaries in perovskite solar cells. *Materials Today Energy* **7**, 149-160 (2018).
18. R. Long, J. Liu, O. V. Prezhdo, Unravelling the effects of grain boundary and chemical doping on electron–hole recombination in CH3NH3PbI3 perovskite by time-domain atomistic simulation. *Journal of the American Chemical Society* **138**, 3884-3890 (2016).
19. T. Niu *et al.*, Stable High-Performance Perovskite Solar Cells via Grain Boundary Passivation. *Advanced Materials* **30**, 1706576 (2018).
20. S. Jariwala *et al.*, Local crystal misorientation influences non-radiative recombination in halide perovskites. *Joule* **3**, 3048-3060 (2019).

21. C. L. Davies *et al.*, Impact of the organic cation on the optoelectronic properties of formamidinium lead triiodide. *The journal of physical chemistry letters* **9**, 4502-4511 (2018).

22. S. K. Yadavalli *et al.*, Mechanisms of Exceptional Grain Growth and Stability in Formamidinium Lead Triiodide Thin Films for Perovskite Solar Cells. *Acta Materialia*, (2020).

23. A. Knight, L. M. Herz, Preventing phase segregation in mixed-halide perovskites: a perspective. *Energy & Environmental Science*, (2020).

24. O. Breitenstein, J. Rakotoniaina, M. H. Al Rifai, M. Werner, Shunt types in crystalline silicon solar cells. *Progress in Photovoltaics: Research and Applications* **12**, 529-538 (2004).

25. A. Stoffers *et al.*, Complex Nanotwin Substructure of an Asymmetric Σ 9 Tilt Grain Boundary in a Silicon Polycrystal. *Physical review letters* **115**, 235502 (2015).

26. Y. Yu *et al.*, Atomic resolution imaging of halide perovskites. *Nano letters* **16**, 7530-7535 (2016).

27. D. Zhang *et al.*, Atomic-resolution transmission electron microscopy of electron beam–sensitive crystalline materials. *Science* **359**, 675-679 (2018).

28. Y. Li *et al.*, Unravelling degradation mechanisms and atomic structure of organic-inorganic halide perovskites by cryo-EM. *Joule* **3**, 2854-2866 (2019).

29. M. U. Rothmann *et al.*, Structural and chemical changes to CH3NH3PbI3 induced by electron and gallium ion beams. *Advanced Materials* **30**, 1800629 (2018).

30. S. Chen *et al.*, Atomic scale insights into structure instability and decomposition pathway of methylammonium lead iodide perovskite. *Nature communications* **9**, 1-8 (2018).

31. R. Hooley, A. Brown, A. Kulak, F. Meldrum, R. Brydson, in *Journal of Physics: Conference Series*. (IOP Publishing, 2017), vol. 902, pp. 012005.

32. K. B. Lohmann *et al.*, Control over crystal size in vapor deposited metal-halide perovskite films. *ACS Energy Letters* **5**, 710-717 (2020).

33. J. Borchert *et al.*, Large-area, highly uniform evaporated formamidinium lead triiodide thin films for solar cells. *ACS Energy Letters* **2**, 2799-2804 (2017).

34. J. Gonnissen *et al.*, Optimal experimental design for the detection of light atoms from high-resolution scanning transmission electron microscopy images. *Applied Physics Letters* **105**, 063116 (2014).

35. L. Oesinghaus *et al.*, Toward tailored film morphologies: the origin of crystal orientation in hybrid perovskite thin films. *Advanced Materials Interfaces* **3**, 1600403 (2016).

36. H. J. Jung *et al.*, Stability of halide perovskite solar cell devices: in situ observation of oxygen diffusion under biasing. *Advanced Materials* **30**, 1802769 (2018).

37. T. W. Kim *et al.*, Self-Organized Superlattice and Phase Coexistence inside Thin Film Organometal Halide Perovskite. *Advanced Materials* **30**, 1705230 (2018).

38. Z. Chen, Z.-G. Gu, W.-Q. Fu, F. Wang, J. Zhang, A confined fabrication of perovskite quantum dots in oriented MOF thin film. *ACS applied materials & interfaces* **8**, 28737-28742 (2016).

39. M. Xiao *et al.*, A Fast Deposition-Crystallization Procedure for Highly Efficient Lead Iodide Perovskite Thin-Film Solar Cells. *Angewandte Chemie* **126**, 10056-10061 (2014).

40. Y. Zhou, H. Sternlicht, N. P. Padture, Transmission electron microscopy of halide perovskite materials and devices. *Joule* **3**, 641-661 (2019).

41. J. Ran *et al.*, Electron-Beam-Related Studies of Halide Perovskites: Challenges and Opportunities. *Advanced Energy Materials*, 1903191 (2020).

42. R. Egerton, Radiation damage to organic and inorganic specimens in the TEM. *Micron* **119**, 72-87 (2019).

43. R. F. Egerton, P. Li, M. Malac, Radiation damage in the TEM and SEM. *Micron* **35**, 399-409 (2004).

44. J. Ran *et al.*, Electron-Beam-Related Studies of Halide Perovskites: Challenges and Opportunities. *Advanced Energy Materials* **n/a**, 1903191.

45. P. A. Beckmann, A review of polytypism in lead iodide. *Crystal Research and Technology* **45**, 455-460 (2010).

46. H.-S. Duan *et al.*, The identification and characterization of defect states in hybrid organic–inorganic perovskite photovoltaics. *Physical chemistry chemical physics* **17**, 112-116 (2015).

47. X. Wen *et al.*, Defect trapping states and charge carrier recombination in organic–inorganic halide perovskites. *Journal of Materials Chemistry C* **4**, 793-800 (2016).

48. D. W. de Quilettes *et al.*, Impact of microstructure on local carrier lifetime in perovskite solar cells. *Science* **348**, 683-686 (2015).

49. Q. Chen *et al.*, Controllable self-induced passivation of hybrid lead iodide perovskites toward high performance solar cells. *Nano letters* **14**, 4158-4163 (2014).

50. Y. Shao, Z. Xiao, C. Bi, Y. Yuan, J. Huang, Origin and elimination of photocurrent hysteresis by fullerene passivation in CH 3 NH 3 PbI 3 planar heterojunction solar cells. *Nature communications* **5**, 1-7 (2014).

51. A. F. Castro-Méndez, J. Hidalgo, J. P. Correa-Baena, The role of grain boundaries in perovskite solar cells. *Advanced Energy Materials* **9**, 1901489 (2019).

52. J. M. Ball, A. Petrozza, Defects in perovskite-halides and their effects in solar cells. *Nature Energy* **1**, 1-13 (2016).

53. A. Merdasa *et al.*, Super-resolution luminescence microspectroscopy reveals the mechanism of photoinduced degradation in CH3NH3PbI3 perovskite nanocrystals. *The Journal of Physical Chemistry C* **120**, 10711-10719 (2016).

54. C. Xiao *et al.*, Mechanisms of Electron-Beam-Induced Damage in Perovskite Thin Films Revealed by Cathodoluminescence Spectroscopy. *The Journal of Physical Chemistry C* **119**, 26904-26911 (2015).

55. J. B. Patel *et al.*, Photocurrent spectroscopy of perovskite solar cells over a wide temperature range from 15 to 350 K. *The journal of physical chemistry letters* **9**, 263-268 (2018).

56. J. D. Zook, Effects of grain boundaries in polycrystalline solar cells. *Applied Physics Letters* **37**, 223-226 (1980).

57. F. Greuter, G. Blatter, Electrical properties of grain boundaries in polycrystalline compound semiconductors. *Semiconductor Science and Technology* **5**, 111 (1990).

58. J.-W. Lee *et al.*, Formamidinium and Cesium Hybridization for Photo- and Moisture-Stable Perovskite Solar Cell. *Advanced Energy Materials* **5**, 1501310-n/a (2015).

59. L. Kimerling, H. Leamy, J. Patel, The electrical properties of stacking faults and precipitates in heat-treated dislocation-free Czochralski silicon. *Applied Physics Letters* **30**, 217-219 (1977).

60. T. W. Kim *et al.*, Self-Organized Superlattice and Phase Coexistence inside Thin Film Organometal Halide Perovskite. *Advanced Materials*, 1705230-n/a.

61. J. Borchert *et al.*, Impurity Tracking Enables Enhanced Control and Reproducibility of Hybrid Perovskite Vapor Deposition. *ACS applied materials & interfaces* **11**, 28851-28857 (2019).